The Astrophysical Journal, 789:25 (20pp), 2014 July 1 doi:10.1088/0004-637X/789/1/25

DYNAMICAL MODEL FOR THE TOROIDAL SPORADIC METEORS

Petr Pokorný[1], David Vokrouhlický[1], David Nesvorný[2], Margaret Campbell-Brown[3], and Peter Brown[3]
[1] Institute of Astronomy, Charles University, V Holešovičkách 2, CZ-18000 Prague 8, Czech Republic; petr.pokorny@volny.cz, vokrouhl@cesnet.cz
[2] Department of Space Studies, Southwest Research Institute, 1050 Walnut Street, Suite 300, Boulder, CO 80302, USA; davidn@boulder.swri.edu
[3] Department of Physics and Astronomy, University of Western Ontario, London, ON N6A 3K7, Canada; margaret.campbell@uwo.ca, pbrown@uwo.ca
Received 2014 January 21; accepted 2014 May 13; published 2014 June 10

ABSTRACT

More than a decade of radar operations by the Canadian Meteor Orbit Radar have allowed both young and moderately old streams to be distinguished from the dispersed sporadic background component. The latter has been categorized according to broad radiant regions visible to Earth-based observers into three broad classes: the helion and anti-helion source, the north and south apex sources, and the north and south toroidal sources (and a related arc structure). The first two are populated mainly by dust released from Jupiter-family comets and new comets. Proper modeling of the toroidal sources has not to date been accomplished. Here, we develop a steady-state model for the toroidal source of the sporadic meteoroid complex, compare our model with the available radar measurements, and investigate a contribution of dust particles from our model to the whole population of sporadic meteoroids. We find that the long-term stable part of the toroidal particles is mainly fed by dust released by Halley type (long period) comets (HTCs). Our synthetic model reproduces most of the observed features of the toroidal particles, including the most troublesome low-eccentricity component, which is due to a combination of two effects: particles' ability to decouple from Jupiter and circularize by the Poynting–Robertson effect, and large collision probability for orbits similar to that of the Earth. Our calibrated model also allows us to estimate the total mass of the HTC-released dust in space and check the flux necessary to maintain the cloud in a steady state.

Key words: interplanetary medium – meteorites, meteors, meteoroids – zodiacal dust

1. INTRODUCTION

The Earth is permanently showered with dust particles born in space. Cometary activity and both cometary and asteroidal breakup events are the natural source processes for these meteoroids. Particles with sizes in the tens of microns to millimeter range are most efficiently detected with powerful radar systems (e.g., Jones et al. 2005). The specular meteor radars (SMRs), such as the Canadian Meteor Orbit Radar (CMOR) and the Advanced Meteor Orbit Radar (AMOR), have provided the most complete information so far in terms of raw numbers of individual orbits for meteoroids impacting the Earth. This is because their observations cover long and often continuous time intervals, and their measurements are able to resolve both the radiant location and velocity of each impacting particle. If properly understood, such observations may tell us much about the source populations of meteoroids, and particularly constrain the overall strength of cometary activity and/or the pace of their breakups.

Analysis of SMR observation data sets allows two components of Earth-impacting meteoroids to be readily distinguished: (1) particles associated with streams concentrated in interplanetary space (e.g., Jenniskens 2006, 2008a, 2008b; Brown et al. 2008, 2010), thus impacting the Earth at discrete and well-defined time windows lasting typically days, and (2) particles belonging to a sporadic background (e.g., Jones & Brown 1993) for an excellent data compilation and a historic perspective). It is believed that the sporadic component is actually composed of particles which originated in streams, which over the course of time have dispersed and become interwoven so much with other sources that they cannot be individually distinguished anymore. Indeed, fine analysis of high-quality data (e.g, Brown et al. 2008, 2010; Campbell-Brown & Wiegert 2009), has allowed an intermediate evolutionary stage between the stream and sporadic components to be identified, namely very broad radiants of long duration, which are still recognizable, particle showers. In this case, the activity from a large but coherent radiant zone in the sky can last up to several months.

In this paper, we focus on the dynamically most processed meteoroid population, namely the sporadic component of meteoroids hitting the Earth. In spite of the fact that sporadic meteoroids impact the Earth from various directions on the sky during the whole year, the geometry of their flux, as seen from Earth, is not isotropic (e.g., Jones & Brown 1993; Campbell-Brown 2008). Rather, they are grouped into certain concentrations of radiants and impact with specific ranges of speeds. This is due to a limited number of source populations for the sporadic particles, combined with Earth's heliocentric motion. Thus, most of the particles observable at the Earth in the sporadic complex belong to one of the three groups: (1) the helion and anti-helion sources, (2) the north and south apex sources, and (3) the north and south toroidal (NT/ST) sources.

The helion and anti-helion sources are the dominant mass flux and therefore they were first to be discovered (e.g., Hawkins 1956). Their radiant concentrations peak on the ecliptic some $\pm 70^\circ$ away from the apex direction, hence nearly pointing toward and away from the Sun. This component has been convincingly interpreted as particles released from the population of Jupiter-family comets (JFCs; e.g., Jones et al. 2001; Wiegert et al. 2009; Nesvorný et al. 2011a). This is only natural, since JFCs are the closest vast population of solar system bodies with significant dust production. It has also been shown that the JFC-produced dust particles contribute dominantly to the thermal flux from the zodiacal cloud as seen by space surveys such as the *InfraRed Astronomical Satellite* (*IRAS*) or *Cosmic Background Explorer* spacecraft (e.g., Nesvorný et al. 2010, 2011a).

The apex source radiants are located at ecliptic latitude $\simeq \pm 20^\circ$ north and south from the apex direction. These particles have been associated with some long-period comets (HTCs) or even new (Oort cloud) comets (OCCs; e.g., Jones et al. 2001;

Wiegert et al. 2009; Nesvorný et al. 2011b; and Section 4.3 here). This is also unsurprising, because both HTCs and OCCs—while being more distant from the Earth—are also very prolific sources of dust in the solar system.

In what follows, we consider the third of the source regions for sporadic meteoroids, namely the toroidal particles. The north toroidal source was first discovered and fully described in the early 1960s from the analysis of Harvard Radio Meteor Project (Hawkins 1962, 1963), with hints coming from earlier projects such as at Jodrell Bank (e.g., Davies 1957; Davies & Gill 1960). Its counterpart, the south toroidal source was confirmed in a study of meteor orbit surveys by Jones & Brown (1993), and later in the more detailed study of AMOR data by Galligan & Baggaley (2005), or Jicamarca high-power large-aperture radar by Chau et al. (2007). The most detailed study of the north toroidal complex so far was presented by Campbell-Brown & Wiegert (2009). An optical component of the north toroidal source was also identified (see, e.g., Hashimoto et al. 2011).

It is interesting, and to some extent actually puzzling, that understanding the parent source for the toroidal particles has proved to be the most difficult of all the sporadic sources. Their apparent source zone on the sky is characterized by high-latitude radiants of $\simeq \pm(55^\circ$–$60^\circ)$, both north and south from the apex direction. The toroidal particles impact the Earth with a typical velocity of $\simeq$35 km s^{-1}. When translated to the parameters of the pre-atmospheric heliocentric orbits, the toroidal particles seen by radars reside on high-inclination orbits with respect to the ecliptic ($\simeq 70^\circ$), have semimajor axes close to 1 au, but with a long tail to larger values, and have a broad distribution of eccentricities with a maximum at $\simeq$0.2 (e.g., Campbell-Brown & Wiegert 2009 and Figure 3 below). Taken straight, there is clearly no significant population of solar system bodies with similar orbits that could provide a significant amount of dust.

Hence, this made previous workers to speculate that either (1) the toroidal particles may come from a single or few, unusual source(s), some of which may be presently extinct, or (2) to conclude that the observed toroidal particle orbits must have significantly evolved from their source regions. The latter might make the source identification somewhat problematic, but there is no a priori reason to believe that the problem should be more complicated than for the helion/anti-helion or apex sources. We shall see in Section 2.1 that an important step before further tracking the zone of origin for the toroidal particles is to apply a proper debiasing, specifically to take into account the collision probability with the Earth for particles on different heliocentric orbits.

1.1. Previous Models

As far as modeling efforts for the origin of toroidal particles are concerned, we note that Jones et al. (2001), in a short but interesting conference paper, assumed the source of the toroidal particles could be interpreted as a high-inclination tail of the JFC-released particles. To prove the concept, they modeled a simple analytic Poynting–Robertson (PR) drag driven evolution from JFC population, but noted that in order to obtain toroidal-source particles they need to significantly push the initial inclination values of this comet population. In particular, instead of having a Gaussian inclination distribution with a standard deviation of $\simeq 11.8^\circ$ (observed), they needed to unrealistically increase this value to $\simeq 28^\circ$ so that the toroidal concentration of radiants would appear in their simulation. While interesting, there is no real physical justification for such a large inclination component among JFCs. Interestingly though, what they started with is roughly an evolutionary phase in our simulations below that identify the starting orbits of the toroidal particles with the HTCs.

Wiegert et al. (2009) presented an effort to explain all major sources of sporadic meteoroids. As far as the toroidal component is concerned, they considered both long-period comets and near-Earth asteroids (NEAs) with high-inclination orbits as potential (immediate) source bodies. Even though interesting, the conclusion from this model suffers significant drawbacks and potential degeneracies. First, the authors did not perform any quantitative fit to the data and hence the modeled orbital distribution of the toroidal particles did not match the observations except in a broad qualitative manner (Figure 4 in Wiegert et al. 2009). More importantly, though, the authors were led to conclude—in contradiction with their initial assumptions—that activity of a single or a few individual objects may dominantly contribute to either of the apparent radiant source regions of meteoroids on the sky. In the case of the NT source region they in fact preferred contribution from several NEAs. This is, however, the weakest point of their model because there is no justification for significant activity from most NEAs as far particle production is concerned (even in the most famous case of 3200 Phaeton, for which a solid evidence of the dust production has been found, e.g., Jewitt et al. 2013, the contemporary amount of dust produced is far too small to account for the associated Geminid stream and in Phaeton's case only occurs because of its unusually small perihelion distance).

In an earlier work, Wiegert (2008) studied the orbital evolution of faint streams with radiants located in the arc structures connecting the toroidal region on the sky with the north and south apex regions (see also Brown et al. 2010). By performing backward integration in time for several of such streams, Wiegert (2008) was able to track their evolution to JFC-like orbits with high inclinations affected by the Kozai–Lidov oscillations. When running forward simulations for particles from such starting orbits (somewhat similar to simpler modeling work of Jones et al. 2001), he concluded that some of them were also capable of populating the toroidal source regions. However, sparse sampling of the initial orbits and/or unavailability of a more advanced collision probability scheme made him conclude that the observed and modeled eccentricity distribution in the NT source still do not match perfectly.

In our work, we revisit the problem of the ultimate source of background particles seen in the toroidal source regions. We are simply returning to the idea qualitatively outlined by Davies & Gill (1960) but equipped with modern observations and better computational speed. These authors hypothesized that the high-inclination and low-eccentricity sporadic NT component ultimately originates from long-period comets. Particles released from them would have a higher chance of overcoming Jupiter's barrier at larger inclinations and would thus be able to migrate into the inner parts of the solar system. Along the way, their orbits would have been circularized by the effects of PR drag. Once on orbits close to the Earth, their collision probability would be so high that they would overwhelm the contribution of their sister particles still residing on high-eccentricity orbits having much longer orbital periods.

1.2. Paper Outline

Our goal is to create a theoretical steady-state model that provides a distribution of orbital elements and velocities of meteors in agreement with observations from CMOR (a brief overview and introductory data analysis is presented in

Section 2). Our numerical model tracks the dynamical evolution of thousands of dust particles in the 100 μm to mm size range released from a synthetic population of HTCs (Section 3.1). We include both gravitational perturbations by planets and relevant non-gravitational effects, namely direct radiation pressure and PR drag. The particle evolution is followed for millions of years until particles reach end of their life, either by being scattered from the solar system by giant planets (mostly Jupiter), hitting one of the terrestrial planets, or evolving too close to the Sun.

The main assumptions and features of the dynamical-evolution model are presented in Section 3.2. Particles in our simulation can also be destroyed because of a collision with other particles of the zodiacal cloud (a simple model is described in Section 3.3). Confining the radiant zone to the NT source as defined by previous studies (e.g., Campbell-Brown 2008), we attempt to adjust free parameters in our model, including the size distribution of the particles at their source (see Section 3.4), to match the observations.

We also attempt to use the CMOR data to absolutely calibrate the population of our modeled particles from HTCs, though we find that this can be presently done only within an order of magnitude (see Section 4). We finally relax the restriction in the model to test particles having to occur in the toroidal-source radiant zone and check the contribution of our modeled HTC dust population to the other source radiant regions on the sky, in particular the north and south apex sources and the arc structure connecting the toroidal sources to the north and south apex sources (Section 4.3). We also check that our estimate of the absolute number of particles from HTCs in interplanetary space does not violate constraints from thermal observations by *IRAS* spacecraft (Section 4.4). General conclusions and an outlook for future work are in the final Section 5.

We note that the architecture of our approach most closely matches the work of Nesvorný et al. (2011a), who considered particles released from JFCs in an attempt to model the helion/anti-helion meteoroid sources, and Nesvorný et al. (2011b), who considered particles released from OCCs in an attempt to model the north and south apex sources.

We should also note that the sporadic toroidal source is known to have the largest temporal variability (even upon removal of the obvious meteor streams; e.g., Campbell-Brown & Wiegert 2009). What we aim to model here is the long-term, time invariant background part of the source, acknowledging that the variable parts need contributions from one or few individual dust-producing bodies (such as the unusual comet 96P/Machholz). Analysis of the time-variable part of the NT source is left to future work. While our model is compared here with data from the CMOR system that can see only the NT source, we believe our results apply equally to the ST source. Consequently, by combining CMOR data with a more sensitive survey, which can also observe the ST sky region (such as the AMOR system), one could potentially improve our results in the future.

2. OBSERVATIONS

We use data recorded in 2012 by the CMOR system (e.g., Jones et al. 2005; upgrades described in Brown et al. 2012), where a filter to remove major meteor showers was applied. We selected radiant and speed information about particles emanating from the NT source, which we define here in accordance with Campbell-Brown (2008), namely, a region centered at 57° north of the apex direction width 15° with in the ecliptic longitude and 9° width in the ecliptic latitude. While there might be slight differences in definition of the NT location across the literature, we believe this is not important for our work provided we use a consistent definition for the data and the model in our analysis. More importantly, our definition clearly separates our sample of NT orbits from the other important sporadic source zones on the sky.

Having made this selection, we are left with a little more than one hundred thousand recorded particles in the NT source by CMOR in 2012. However, to be conservative, we opted to discard all inputs that have (1) geocentric velocity uncertainty $\geqslant$4 km s^{-1} and (2) radiant position uncertainty $\geqslant 2^\circ$. Here the individual radiant and speed uncertainties are found using a Monte Carlo procedure described in Weryk & Brown (2012).

Using this quality filter, the sample dropped by roughly one half to 56,898 meteors detected during the calendar year 2012. Most of the discarded particles had low signal-to-noise ratios and were at the edge of detectability of the CMOR system (generally small particles). In order to characterize the detection sensitivity of the system, Wiegert et al. (2009) introduced an ionization factor

$$I = \frac{m}{10^{-7}\,\mathrm{kg}} \left(\frac{V}{30\,\mathrm{km\ s^{-1}}} \right)^{3.5}, \qquad (1)$$

where m is the particle mass and V its apparent velocity at the Earth (composed of the relative velocity at intersection of the particle's heliocentric orbit with the Earth and the planet's velocity vector including acceleration due to gravity). Particles with I larger than some critical threshold $I_\star$ are detected, while those with I smaller than $I_\star$ produce too little ionization in the atmosphere to be detected by the radar. While necessarily approximate, the ionization factor-based detection criterion is a useful tool for our modeling work in order to select modeled impacting particles that could be recorded by the system. We note that $I_\star$ actually varies over the sky, being a function of echo range and position in the CMOR antenna beam pattern—here we refer to the absolute minimum $I_\star$, which for CMOR occurs at the zenith. The numerical constants in (1) have been purposely chosen such that $I_\star \simeq 1$ for the CMOR system. While upgrades may decrease somewhat this value a little, we observe that the ionization factor values of the selected NT particles that passed our tightened criterion on radiant and impact velocity uncertainties sharply drop at $\simeq$1. This confirms that the limiting value $I_\star \simeq 1$ is appropriate for our work.

Figure 1 shows a correlation between the size D of the detected NT particles and their apparent impact velocity V. We assumed a bulk density of 2 g cm^{-3} to convert the reported masses m to effective particle sizes. Masses are computed by calculating the electron-line density q of the echo based on its received power, location in the radar beam and range. The mass–velocity–ionization relation of Verniani (1973) is then used to convert from q to m. Particles smaller than $\sim$200 μm were not detected in the NT source because their typical impact speeds make the ionization factor I smaller than $I_\star$. Indeed, we observe a strong D versus V correlation whose low-end closely follows the $I \simeq I_\star \simeq 1$ limit. This prevents small particles with $D \leqslant 500\,\mu$m traveling at low speeds, from being detected. The recorded data does not show any signs of an upper ionization cutoff, which indicates that CMOR detects large and fast particles as well.

Figure 2 shows the number of recorded NT particles in our sample as a function of the solar longitude λ at detection, or equivalently, the temporal flux of the NT particles in 2012. Previous studies (e.g., Campbell-Brown & Wiegert 2009 and

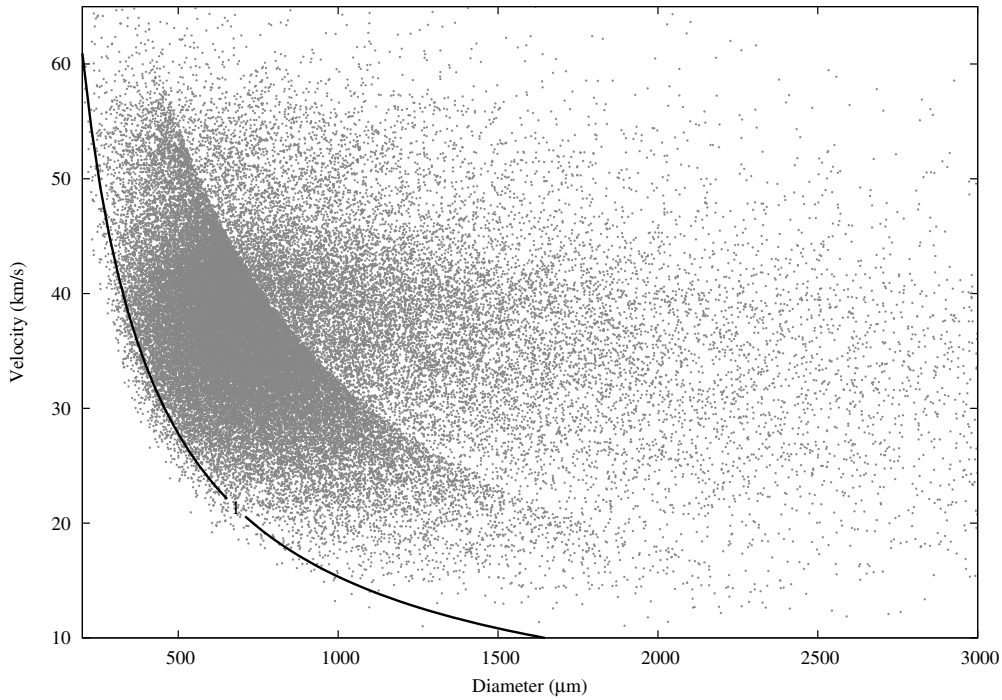

Figure 1. Selected north toroidal source particles recorded by the CMOR system during the year 2012: effective size D (in μm) vs. impact velocity V (in km s^{-1}). Isoline of a constant ionization factor (Equation (1)) for $I = I_\star = 1$, shown by the solid line, roughly delimit the range of detected particles. The discontinuity in apparent numbers running parallel to the $I_\star = 1$ line represents the approximate transition point between underdense and overdense echoes.

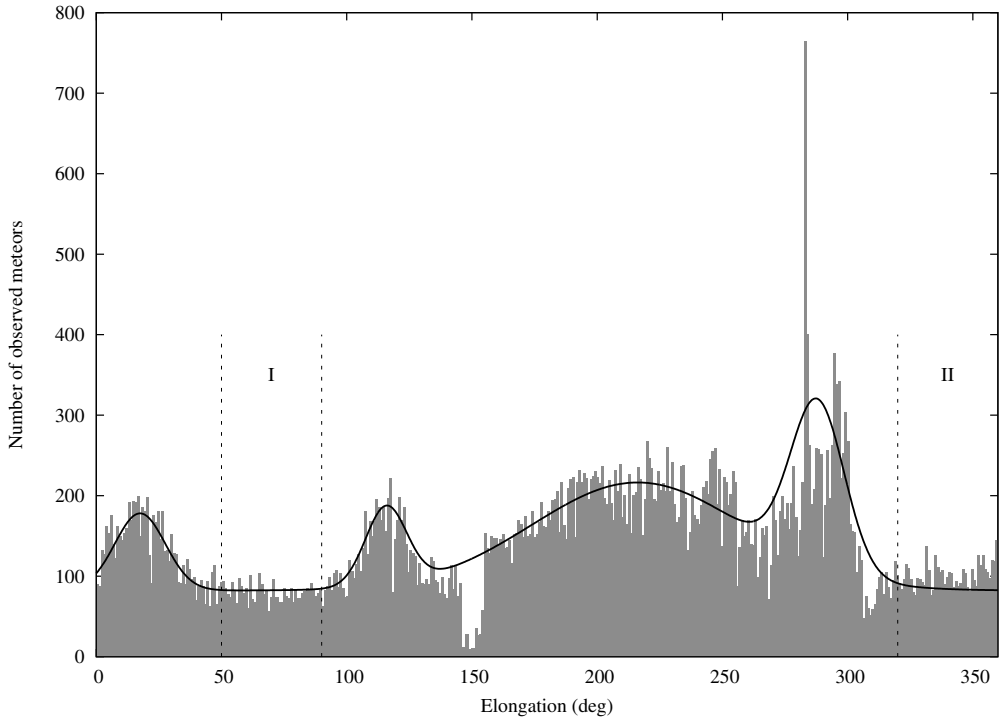

Figure 2. Selected north toroidal source particles recorded by the CMOR system during the year 2012: daily impact statistics vs. solar longitude λ. The solid black line, composed of a constant—background—term and four broad Gaussian contributions, depict an envelope model for activity in the NT source (compact streams such as Quadrantids at $\lambda \simeq 283^\circ$, and θ and ξ Coronae Borealids at $\lambda \simeq (285^\circ$–$300^\circ)$ are not considered in this fit). The intervals labeled I and II, delimited by dashed lines, are our primary representation of the background, steady-state component in the source.

references therein) noticed and characterized significant variability in the source which is also immediately seen in this figure. However, in this work, we shall not study fine details of the source variability. Our assumption is that the source has its own permanent (steady-state) activity over which contributions from individual source(s) overlays. In this work we plan to model the primary, presumably long-term stable, component. Obviously, it is not easy (if even possible) to rigorously separate the steady and variable components. Here we take a simple approach and proceed as follows.

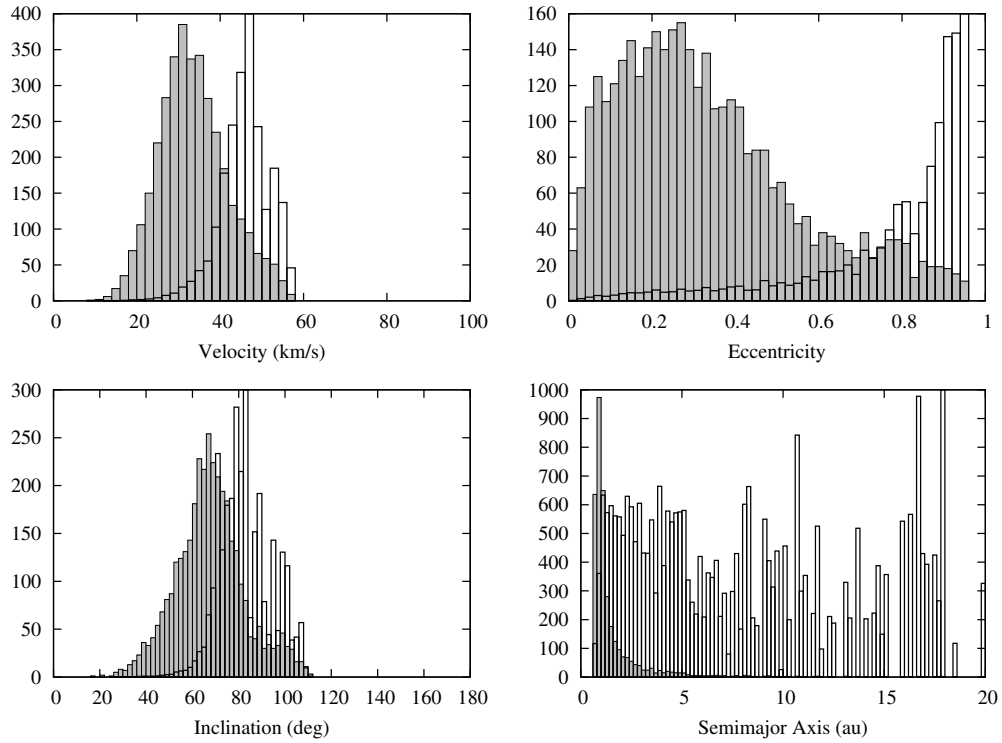

Figure 3. Distribution of geocentric impact speed (top left), eccentricity (top right), inclination (bottom and left), and heliocentric semimajor axis (bottom right) for 3550 selected particles of the background population of NT particles. The gray histograms correspond to the observed data from CMOR. The unfilled black histograms were constructed using the methods described in Section 2.1 and approximate the distribution of the population with an ability of generating observed NT particles normalized to unity. The raw and generating distributions are significantly different, implying there are strong selection effects in the observed population. The parameters of the generating population led us to choose HTCs as the most promising source of NT particles.

First, we recognize that there are two principal strong stream contributions in the NT source, namely: (1) Quadrantids at $\lambda \simeq 283^\circ$, and (2) θ and ξ Coronae Borealids at $\lambda \simeq (285^\circ$–$300^\circ)$. These are the sources H and I described in Campbell-Brown & Wiegert (2009). Next, there are roughly four broader, more dispersed stream contributions named Helion and Antihelion Arc and B as given in Campbell-Brown & Wiegert (2009) throughout the course of the year. In our data (Figure 2) we can see them as roughly Gaussian features at solar longitude of $\sim 17^\circ$, $\sim 115^\circ$, $\sim 216^\circ$ and $\sim 280^\circ$ (the last has been also described by Brown et al. 2010, as an underlying Quadrantids extension consisting of the November ι Draconids and December α Draconids, perhaps indicating an old stream complex related to activity of the comet 96P/Machholz). The total duration of this complex is one to two months. We find it interesting that these four broad features may actually be organized in two pairs with longitude difference of $\simeq (180^\circ$–$200^\circ)$. Hence at least two different individual sources are needed, out of which the pair consisting of the toroidal D stream and the Quadrantid broad underlying stream have a likely progenitor in the activity of comet 96P/Machholz several thousand years ago (e.g., Gonczi et al. 1992; Jones & Jones 1993; Sekanina & Chodas 2005; Kaňuchová & Neslušan 2007). We shall address this issue in a forthcoming study.

To avoid confusion between background and individual sources we are then left with two longitude intervals apparently devoid of stream activity: (1) $\simeq (50^\circ$–$90^\circ)$, and (2) $\simeq (320^\circ$–$360^\circ)$. Campbell-Brown & Wiegert (2009) describe a weak and very broad toroidal source C in the latter interval, while no recognizable individual source is seen in the first interval. As a result, we shall consider NT particles in the first interval (1) to be our primary test sample of background population. Tests show, however, that orbital data for particles in the second interval (2) are very similar to those in the first interval (1), so we feel justified in checking our results by merging information from both intervals of time. Our restricted sample of background NT-source particles contains 3550 individual meteoroid orbits, roughly 90 particles hitting the Earth per day.

Figure 3 (gray histogram) shows the distribution of the apparent impact speed of the selected NT particles and distributions of the orbital elements, namely semimajor axis, eccentricity and inclination. Our results are very similar to those of Campbell-Brown (2008) or Campbell-Brown & Wiegert (2009). The most distinct features are: (1) semimajor axis distribution peaked at 1 au, (2) broad eccentricity distribution with a predominance of low-eccentricity orbits (eccentricities smaller than ~ 0.4), and (3) characteristic inclinations between 60° and 70° with a tail to retrograde orbits (correlated with a velocity-distribution tail to values larger than ~ 45 km s^{-1}). Data in the second interval (2) described above show only a very small excess of larger-eccentricity orbits relative to period (1). A more detailed study of the data set may be found in the Appendix.

2.1. Searching for the Generating Population

Before we formulate our model and compare its results with the observations of the background NT particles, we first perform a simple analysis of the observed NT meteoroid sample selected in the previous section.

Our first step is to debias the observed population for impact probability with the Earth. This is an important factor because a body on a given heliocentric orbit with semimajor axis a, eccentricity e and inclination i has a mean collision probability $P_{\rm coll}$ with the Earth that strongly depends on these parameters. Since we aim to model the steady-state, background

population, we can use collision probability values averaged over a long-enough time interval (characteristic of the variation of the orbital longitudes of node and pericenter—typically of order 10^4 yr for NT particles). Obviously, an underlying hierarchy in the orbital time evolution is assumed here, notably that the secular angles change faster than the semimajor axis changes due to radiation drag. While this may not always be satisfied for individual particle orbits, such an assumption holds population-wise.

Traditionally, workers adopted Öpik-type theory for $P_{\rm coll}$ (e.g., Öpik 1951), or equivalent variants that only allow for slight eccentricity of the target planet (e.g., Wetherill 1967; Greenberg 1982). However, the dynamics of the high-inclination orbits which dominate in the NT source violate the assumptions of all these approaches by being strongly affected by the Kozai–Lidov cycles (e.g., Kozai 1962). This motivated us to formulate a new secular collisional probability approach that takes into account at least the fundamental elements of the Kozai–Lidov effect (Vokrouhlický et al. 2012; Pokorný & Vokrouhlický 2013). While still approximate (it does not take into account the orbit's ability to be scattered by Jupiter if close encounters to that planets are possible), the new theory represents an important improvement over previous ones. Not only is a refined value of $P_{\rm coll}$ obtained, which for some sets of orbital elements may be similar to unrefined value and for another set the difference may be higher than an order of magnitude, but also a correct representation of the radiant position at intersection with the Earth is calculated.

For that reason we always use our new formulation of $P_{\rm coll}$ in this paper. In fact, a faster variant from Vokrouhlický et al. (2012), where the target planet is assumed to be on a circular orbit, is fully sufficient for our work.

We can now debias the population of particles observed from the NT source by representing a single input of each particle seen to impact from a heliocentric orbit with (a, e, i) elements with a weight $\propto 1/P_{\rm coll}$ and obtain a population of particles with an ability to generate observed NT orbits. Figure 3 (black open histograms) shows the results. The generating population is very different from the observed one. The semimajor axis values distribution is basically flat up to Jupiter's heliocentric distance of $\simeq 5$ au, followed by a slow decrease in numbers at larger values. There is still a fair contribution of orbits with a beyond 10 au, though both noise (due to few observed orbits with those values of a) and imperfection in $P_{\rm coll}$ determination affect the distribution trend. In the same way, the generating eccentricity steadily increases to large values, indicating the low-eccentricity population is just a minor part of the whole distribution. The inclinations, while constrained by the relatively tight radiant zone on the sky, are also slightly shifted to larger values, now having a higher contribution of retrograde orbits. This is also reflected in systematically larger impact velocities for the generating population. All these findings point to a cometary origin of the NT particles. Since JFC orbital parameters are not compatible with the orbital elements of generating particles seen in Figure 3, especially as far as the semimajor axis and inclination are concerned, we are left with the long-period comet population. The contribution of the new comets has been studied by Nesvorný et al. (2011b), who showed that the isotropic and more distant initial orbits preferentially led the dust particles impacting in the apex sources. We thus suggest that the prime candidate source population for the NT particles are HTCs. In Sections 3 and 4 we explore this hypothesis with a detailed numerical model.

3. MODEL: THEORETICAL BASIS

Our model contains the following elements. We start with a description of the assumed ultimate population of source bodies from which the NT particles are initially released. To that end we use an up-to-date synthetic model of HTCs (Section 3.1). The orbital evolution of particles with different sizes is numerically propagated until it reaches one of several possible end-states (ejection from the solar system or impact on the Sun or planets; Section 3.2). The integrator accounts for both gravitational perturbations due to planets and radiative effects (direct solar radiation pressure and PR drag). Evolutionary paths for all particles are stored and used for further analysis. The effects of collisional destruction by impacts of other zodiacal cloud particles are modeled separately using a Monte Carlo probabilistic scheme (Section 3.3). Proper weighting of the contribution from particles with different sizes is also needed (Section 3.4). Merging the data together to simulate the synthetic impact population at NT source and comparison with observations is covered in Section 4.

3.1. HTC Model: Initial Particle Orbits

We adopt results from Levison et al. (2006). These authors developed a steady-state model for HTC orbital architecture, assuming they originate in the scattered disk. Tracking the orbital evolution of a large number of test particles, their model was able to successfully match the observed distribution of HTC orbital elements, including the most problematic case of the inclination distribution that was not reproduced in previous efforts. This is because the observed inclination distribution of HTCs contains preferentially prograde orbits with a median inclination value of $\sim 55^\circ$ and only a small fraction of comets on retrograde orbits (Figure 4). In relation to the HTC dust it is thus interesting to note that previous works, such as Wiegert et al. (2009), appeared to focus on the role of famously known long-period comets such as 1P/Halley or 55P/Tempel-Tuttle, whose orbits are actually outliers in their group. We also note that nearly half of HTCs have inclination values between $\sim 40^\circ$ and $\sim 80^\circ$, which additionally favors them as a source for NT (and ST) particles.

The starting orbits for our particles are those of the synthetic, steady-state population of HTCs from Levison et al. (2006). Since we take into account radiation forces, including direct radiation pressure and PR drag, in the particle dynamics, the osculating orbits upon release from the parent comet change (e.g., Dermott et al. 2001). This is because radiation pressure effectively changes the solar mass M to $M\,(1-\beta)$, with

$$\beta = 1.15\,\frac{Q_{\rm pr}}{\rho D}\,, \tag{2}$$

for a particle of a bulk density ρ (in g cm^{-3}) and size D (in μm). Details of the radiation interaction with the particle are included in the pressure coefficient $Q_{\rm pr}$. In all our simulations below we take $\rho = 2$ g cm^{-3} and set $Q_{\rm pr} = 1$ for simplicity. One of the solar mass recalibration aspects is that particle orbits may become unbound when released from a high-eccentricity cometary orbit (Figure 4). To stay initially bound in the solar system, a particle with a beta factor β must be released at heliocentric distance R

$$R > R^\star = 2\beta a\,, \tag{3}$$

for a cometary orbit with a semimajor axis a (e.g., Dermott et al. 2001). Since the particles of interest for us have typically

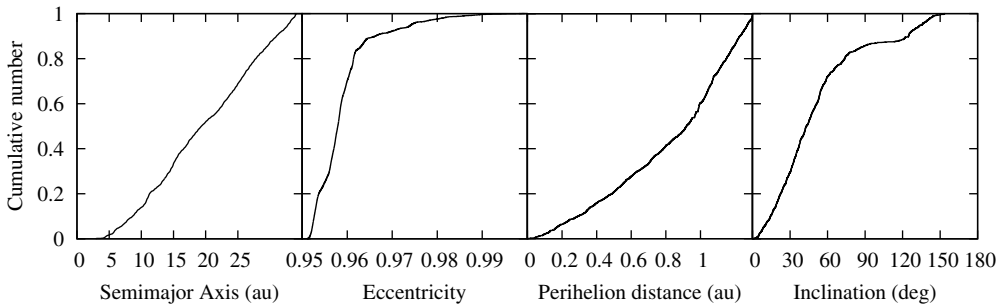

Figure 4. Distribution of the heliocentric orbital elements of the synthetic population of HTCs: semimajor axis a (left), eccentricity e (second from left), perihelion distance q (second from right), and inclination i (right). Most notably, the inclination is unevenly distributed about 90°: the median inclination of HTCs is ∼55° and only ∼20% of orbits have inclination larger than 90°. This favorably directs particles surviving the Jupiter barrier to the toroidal source zone.

$D \geqslant 200\,\mu$m, as suggested by Figure 1, the condition (3) is not very restrictive (it only prohibits release very near perihelion for comets with the largest a and our smallest particles). To keep things simple, since our model contains enough free parameters of more importance, we release particles uniformly in mean longitude along the cometary orbits (not seeking thus an additional parameterization to model their ejection as more concentrated toward perihelion). We also give the particles zero ejection velocity with respect to the comet, accounting only for the radiation pressure effects mentioned above.

The starting orbits of our particles have different perihelion distances q in accord with the distribution shown on the third panel in Figure 4. Comets with smaller q values are generally more active and may deliver more dust particles to interplanetary space. In order to account for this bias, we introduce a weighting factor $W_{\rm a}$, assigned to each of the particles as

$$W_{\rm a} = q^{-\gamma}\ . \tag{4}$$

Here q is in astronomical units and γ is an adjustable parameter of our model. We nominally set $\gamma = 0$, but test the sensitivity of the results to adopting positive γ values.

It is also important to note that we consider a population of starting orbits with perihelion q up to a maximum value of 1.3 au (Figure 4). However, selecting a limited number of particle sizes, we also tested a solutions with q extending to 2.6 au, extrapolating the trend from the Levison et al. (2006) model. We found that the results are not sensitive to this limit and are comparable to our main results. For that reason we believe that the limitation of $q \leqslant 1.3$ au does not represent a limitation of our model.

3.2. Orbital Evolution Propagator and Results of Particle Integrations

The particle orbits were numerically propagated using the `swift_rmvs3` code (e.g., Levison & Duncan 1994; http://www.boulder.swri.edu/∼hal/swift.html) which allows an efficient long-term integration of test bodies in the solar system. Gravitational perturbations from all planets, whose initial orbits were obtained from the JPL DE405 ephemerides, were taken into account. The radiation forces were implemented in two steps upon evaluation of the β-factor for particles of a specified size (Equation (2)): (1) the direct radiation pressure was represented as the appropriate recalibration of the solar mass, and (2) the PR drag was introduced as a perturbation like the gravitational effects of planets. The code was tested and successfully used in previous studies (e.g., Nesvorný et al. 2006, 2010, 2011a, 2011b). We also take into account the drag effect of the solar wind which is, on average, believed to increase the PR drag by some 30% (e.g., Dermott et al. 2001).

Since we aim to model a steady-state population of HTC-related particles in interplanetary space, once started on their initial orbits, the particles were followed until the whole population was eliminated. There were several orbital end-states in our simulations. Close encounter with giant planets, mainly Jupiter, could eject the particles from the solar system (we consider this condition to be when the heliocentric distance of the particle becomes larger than 10,000 au). Particles may also hit the Sun or its immediate vicinity. We eliminate them when the heliocentric distance becomes smaller than 0.05 au, roughly ten solar radii. Below that distance the effective temperature of the particles exceeds ∼1300 K and the particles are deemed to evaporate or be torn by thermal stresses (e.g., Čapek & Vokrouhlický 2010). Some particles may even hit a planet, including the Earth, but the likelihood is small given a limited number of integrated bodies. We do not make use of the directly simulated Earth impacts in our analysis.

Since all planets, including Mercury, are propagated together with the dust particles in our simulations, we use a short timestep of 1 day. In order to prevent disk overflow, the particle orbits are exported, and used for further analysis, once every 100 yr in all our simulations. We ran simulations for particles of different sizes D, namely, 100 μm, 200 μm, 400 μm, 600 μm, 800 μm, 1000 μm, 1200 μm, 1500 μm, and 2000 μm. Each time, we had 20, 000 randomly generated orbits of particles, giving altogether nearly 200,000 propagated particles. Most of the runs were completed by $t = 10$ Myr, and only some of the largest particles lasted longer in our simulations. We found that the dynamics of particles in our two largest-size bins is sufficiently similar to bin them together. This means trajectories of our largest particles, 2 mm in size, could be taken as a good template for dynamics of any other particles with larger size. Data shown in Figure 1 indicate that we do not need to integrate orbits for particles with sizes smaller than 100 μm for this project as this is below the sensitivity limit for CMOR. With our choice, and computer-power limitations, we believe we sufficiently covered the necessary interval of particle sizes for the population size distribution analysis (Section 3.4).

In the zero approximation, the population depletion with time t in our runs may be matched by an exponential law $\propto \exp(-t/\tau)$, where τ is some characteristic timescale. For our smallest particles of 100 μm and 200 μm we found $\tau \simeq 0.67$ Myr and $\tau \simeq 1.07$ Myr, respectively. For all larger particles, the τ value ranged between ∼1.48 Myr and ∼1.85 Myr, quickly approaching a limiting value of ∼1.9 Myr. This information is necessary when estimating the production rate of HTC

particles at the source to maintain a steady-state situation (see Section 4).

Another interesting piece of information that we obtain from our simulations relates to the particles ability to decouple from the gravitational influence of Jupiter and migrate inward to the terrestrial planet zone. We find that ∼25% particles of 200 μm size decouple from Jupiter, while only ∼5% of 1 mm particles are able to do so. These percentages are large and promising for the modeling of the toroidal sources. Note that similar integrations for particles released from the Oort cloud comets revealed that less than ∼0.1%–0.5% of particles decouple from Jupiter in this size range (e.g., Nesvorný et al. 2011b). This is more than a factor of 10 fewer particles than in our simulations of HTC-born particles.

3.3. A Simple Implementation of the Particle Collisional Lifetime

Particles may also be removed on their way toward the inner solar system because of a collision with another particle in the interplanetary space. This effect is not directly modeled in our numerical simulations and must be considered separately. Indeed, the estimated collisional lifetime for particles in the relevant size range (Figure 1) may be shorter than the characteristic dynamical lifetime mentioned above, especially when particles move to inside part of the Jupiter's orbit. For reference, a $D \sim 1$ mm particle on $a \sim 1$ au orbit, typical for the NT source zone (Figure 3), has an estimated collisional lifetime $\lesssim 10^5$ yr (e.g., Steel & Elford 1986; Grün et al. 1985). This may be up to an order of magnitude shorter than the dynamical transport time from its initial, HTC-like orbit.

Similarly to Wiegert et al. (2009), we used the collisional model of Steel & Elford (1986, hereafter SE86), first checking that similar results would also have been obtained with the model by Grün et al. (1985) that has been used by Nesvorný et al. (2011a, 2011b). Conveniently, the SE86 model provides the dependence of the collisional lifetime on the orbital elements of the particle, including the inclination value, which was our largest concern in this study. In order to estimate the collisional lifetime of a particle, SE86 use a technique of volume integration of partial space–density distribution functions of (1) the zodiacal cloud model, and (2) that of particle-orbits swept during one secular cycle of node and pericenter longitudes (see Kessler 1981). There are obviously large approximations taken both in (1) and (2). As far as (1) is concerned, SE86 use a very simple density distribution model of the zodiacal cloud (Equation (2) in SE86). We adopt this model as well. As far as (2) is concerned, SE86 assume constant eccentricity and inclination values during the secular cycle. This is particularly violated for the high-eccentricity and high-inclination orbits studied here, and thus we have slightly modified the SE86 technique. In particular, we evaluate an instantaneous collision probability of the particle orbit with the zodiacal cloud performing simply a one-dimensional averaging orbit revolution about the Sun (some details are given in Supplementary materials). This result better suits our model, because we can now fully account for nontrivial secular variations of the particle orbit as provided by our numerical integrator. Moreover, we model the collisional dynamics of the particles using a Monte Carlo model with a timestep shorter than the orbital secular cycle, so the estimate of a collisional lifetime for the instantaneous orbit would be needed anyway. As far as the size dependence of the collisional lifetime is concerned, we assumed that projectile capable of breaking a given particle is one ∼30 times smaller in size (SE86) and used the zodiacal cloud size distribution from Grün et al. (1985). Obviously, all these assumptions are grossly simplified. For that reason we also used an empirical factor $F_{\rm coll}$ by which we multiply the estimated collisional lifetime. Values of $F_{\rm coll}$ between 1 and 30 are allowed in our procedure and adjusted to obtain the best match between the observations and the model (Section 4; Nesvorný et al. 2011a, 2011b have used a similar scheme of extending the canonical collisional lifetime values).

We implement the effects of a finite collisional lifetime in the following way. Our numerical integration of the particle-orbital evolution treats them as indestructible bodies and outputs the state vectors once every $dt = 100$ yr. In the modeling phase, we load these orbital histories and follow the particles anew. At this phase, though, we assume a finite collisional lifetime $\tau_{\rm cl}$ and at each timestep dt we consider a probability $1 - \exp(-dt/\tau_{\rm cl})$ that the particle collisionally disrupts. At each timestep we thus consider a randomly generated number, compare it with the disruption probability and decide whether the particle is to be eliminated from further analysis. Since such a Monte Carlo procedure brings a stochastic element in our work, and computer power allows only a small number of particles to be analyzed, we typically repeat the analysis 25 times and average over the results.

We should also point out that in this work, as well in all previous works, the particles deemed to collisionally disrupt are fully eliminated. In reality, though, disruption events form fragments that themselves continue orbital evolution and eventually may contribute to the observed signal at the Earth. We believe that the $F_{\rm coll} > 1$ values which best suit in our model (Section 4) effectively account for the fragment contribution at the zero level. In other words, the $F_{\rm coll} > 1$ values might not be in great conflict with the $\tau_{\rm cl}$ values estimated by SE86 and Grün et al. (1985).

3.4. Assumptions About the Size Distribution of Particles at Their Source

Particles of different size D may take different orbital evolution paths and thus contribute in an uneven way to our results. We thus need to run our simulations for a set of different sizes and then combine the data. The underlying weighting procedure has to account for the size frequency distribution (SFD) of the particle population. Except for Section 2.1, we always work in this paper with the SFD at the ultimate source in the solar system, i.e., corresponding to the particle population freshly released from the parent comets. The source SFD reported here is not equal to that of the Earth-impacting particles that is affected by both dynamical (PR drag) and physical (collisions) effects. Our model takes these alterations into account.

While the particle SFD may be a complicated function of D in principle, experience shows that a broken power-law representation is a fairly good approximation unless the size range ($D_{\rm min}$, $D_{\rm max}$) is too large. Figure 1 provides guidance for the selection of these limits. Namely, we consider $D_{\rm min} \simeq 200\,\mu$m, because basically no smaller particles are recorded in our sample due to the ionization factor cutoff $I \geqslant I_\star$ described above. Similarly, we take $D_{\rm max} \simeq 3$ mm, because particles larger than this value are rarely detected by CMOR or have long-duration echo characteristics which do not allow automatic orbit determination by CMOR in the NT source.

The most general SFD we test in our work allows a breakpoint between piece-wise power laws at a midpoint[4] $D_{\rm mid} \in$

[4] We may also use a single-slope power-law SFD by setting $\alpha = \beta$ in all formulas in Sections 3.4 and 4.2; one easily verifies that $D_{\rm mid}$ is either arbitrary or drops out of the equations in that case.

$(D_{\rm min}, D_{\rm max})$. In particular, at larger sizes $(D_{\rm mid}, D_{\rm max})$ we assume a power law with a differential size distribution exponent α:

$$dN = N_\alpha \left(\frac{D_{\rm max}}{D}\right)^\alpha \frac{dD}{D_{\rm max}} , \quad (5)$$

while at smaller sizes $(D_{\rm min}, D_{\rm mid})$ we assume a power law with a differential size distribution exponent β:

$$dN = N_\beta \left(\frac{D_{\rm mid}}{D}\right)^\beta \frac{dD}{D_{\rm mid}} . \quad (6)$$

To ensure continuity in population statistics we must choose $N_\beta = N_\alpha\,(D_{\rm max}/D_{\rm mid})^{\alpha-1}$. Cumulative SFD functions, compatible with differential distribution laws from Equations (5) and (6), are given by

$$N(>D) = N_0 \left(\frac{D_{\rm max}}{D}\right)^{\alpha-1} , \quad (7)$$

for $D \in (D_{\rm mid}, D_{\rm max})$ and

$$N(>D) = \frac{N_\beta}{\beta-1}\left(\frac{D_{\rm mid}}{D}\right)^{\beta-1} + C_1 , \quad (8)$$

for $D \in (D_{\rm min}, D_{\rm mid})$. Here we introduced a constant

$$C_1 = \frac{N_\beta}{\beta-1}\frac{\beta-\alpha}{\alpha-1} , \quad (9)$$

and additionally made a choice $N_\alpha = N_0\,(\alpha-1)$ with a free parameter N_0 in Equation (9). One convenience of doing so is good behavior of the cumulative SFD at $D = D_{\rm max}$. The SFD model is three-parameter, with adjustable constants being (1) N_0, fixing the absolute number of particles with $D = D_{\rm max}$, and (2) exponents α and β. We only require (and expect) both α and β be larger than unity, with an expected value between 3 and 4. A starting point for these values come both from direct comet observations (see, e.g., compilation of data by Fulle 2004) and mass–index calculations for the core of young meteoroid streams (e.g, Blaauw et al. 2011). The total number of particles $N_{\rm tot}$ in the specified range of sizes reads $N_{\rm tot} = C_1 + C_2$, with

$$C_2 = \frac{N_\beta}{\beta-1}\left(\frac{D_{\rm mid}}{D_{\rm min}}\right)^{\beta-1} . \quad (10)$$

While the above formulation enforces continuity of the cumulative SFD across the whole range of sizes, the finite range of the two intervals $(D_{\rm min}, D_{\rm mid})$ and $(D_{\rm mid}, D_{\rm max})$ produce boundary effects. In particular, performing a least squares fit of the single power-law exponent in each of the intervals may not result in either α of β values, which formally define our broken power-law SFD. The effective power-law exponent may be steeper or shallower, and the boundary effect is larger for a smaller range of sizes (and example of the phenomenon is discussed in the Supplementary materials). We shall bear this in mind when commenting on our formal solutions for α and β in Section 4.

In our procedure, we follow the orbital evolution of a set of sizes $(D_i, i = 1, \ldots, n) \in (D_{\rm min}, D_{\rm max})$.[5] The population weight assigned to each of the sizes is determined as follows: (1) we divide intervals between the neighbor sizes in half, taking a logarithmic size scale, and (2) use the cumulative SFD in (7) and (8) to determine the number of population particles N_i in the interval centered at the chosen size D_i. Were we able to integrate a large number of sizes, and the SFD were just a single power law with and index α, we would have $N_i \propto D_i^{1-\alpha}$ (compare with Wiegert et al. 2009, Section 2.2.1). The finite number of sizes D_i, and the assumed broken power law of SFD, may change this simple dependence. The estimated population number N_i is used in our fitting procedure as a weighting factor $W_{\rm d}$ assigned to each of the particles of a given size D_i: $W_{\rm d} = N_i$.

[5] In our case, $n = 9$ and the individual sizes D_i were listed in Section 3.2.

3.5. Particle Weighting Together and Fitting Model Parameters

Summarizing the information above, a total weight W is assigned to each particle in our simulation, composed of three partial terms:

$$W = W_{\rm a}\, W_{\rm c}\, W_{\rm d} . \quad (11)$$

The first contribution, $W_{\rm a}$, represents the activity of the source comet in terms of particle production (Section 3.1). The second contribution, $W_{\rm c}$, is the collision probability of the particle orbit at a given time with respect to the Earth. We take $W_{\rm c} = P_{\rm coll}$, where $P_{\rm coll}$ is from Vokrouhlický et al. (2012). The last contribution, $W_{\rm d}$, expresses the increasing number of small particles in the population through the SFD modeling described in Section 3.4. Recall that the fitted SFD is representative of the source population of particles released from HTC.

We assume that our modeled particle population from HTC is in an approximate steady state. This allows us to neglect the time evolution of the individual particles in our simulation since any time should be equally representative of the population state. Rather, we just perform a direct summation of the particle contributions to the impacting population onto the Earth over all computer-stored orbital states of all particles.

Our goal is to examine the hypothesis that the particles released from HTCs represent a viable explanation of the background population of NT meteoroids as seen by the CMOR system. To that end we match the observed particle population, as described in Section 2, to the synthetic population, as obtained with our model in Section 3. In doing so we adjust several free parameters introduced above, namely, (1) SFD slope parameters α and β, break-point location $D_{\rm mid}$ and number N_0 of particles with the largest size $D_{\rm max} = 3$ mm (if fitting only a single-slope power-law SFD we adjust α and N_0), (2) particle production slope parameter γ from Equation (4), and (3) empirical adjustment parameter $F_{\rm coll}$ of the collisional lifetime of particles in the interplanetary space (Section 3.3). This makes in total six free parameters at most (fewer if we decide, for instance, to use just a single-slope power-law SFD representation). We also found it useful to substitute for the N_0 parameter a parameter $F_{\rm imp}$ defined as follows. Having chosen a set of the above mentioned parameters we predict $N_{\rm imp}$ particles impacting in the selected interval of solar longitudes (Section 2) and being detected by CMOR (more of the detection sensitivity in Section 4.2). Ideally, N_0 should assure $N_{\rm imp}$ equals number of truly detected particles $N_{\rm obs} = 3550$ (Section 2). However, to cope with small imperfections of the model and our simplifications in fully modeling the CMOR system response function, we introduce a scaling factor $F_{\rm imp} = N_{\rm imp}/N_{\rm obs}$ and allow its values to range in some reasonable interval around unity.

Our target function may be either one (or a combination) of the orbital element or velocity distributions shown on Figure 3. Denoting R_i the observed data and S_i the modeled data, we use of a chi-square function

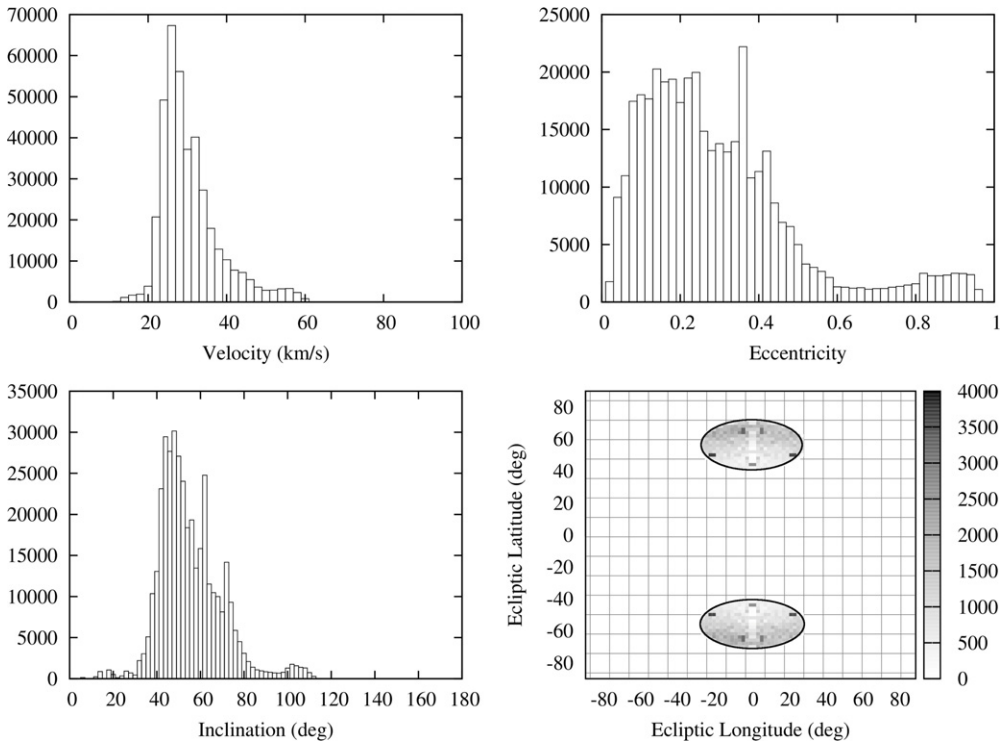

Figure 5. Synthetic NT population of particles with $D = 200\,\mu$m from the sole dynamical transport of HTC-like orbits at origin: infinite collisional lifetime are assumed and no lower cutoff in the ionization factor I at impact (i.e., effectively $I_\star = 0$). Distribution of geocentric impact speed V (top left), eccentricity e (top right), and inclination (bottom left) at impact, all weighted by the collision probability $P_{\rm coll}$. Distribution of radiant locations restricted to the NT and ST zones (bottom and right). Only meteors in two elliptical regions in the bottom and right panel are taken into account. The grid shows the radiant locations that were not considered. PR drag makes the orbital eccentricity decrease significantly from the initial values, and orbits with larger than $\sim 80^\circ$ inclination typically impact the Sun on their way to the inner solar system due to the Kozai–Lidov effect.

$$\chi^2 = \sum_i \frac{(R_i - S_i)^2}{R_i} \tag{12}$$

to evaluate the similarity of the observed and modeled data (see also Press et al. 2007). The goodness of fit is best represented with ξ^2 normalized by $N - m$, where N is number of data (bins) and m is the number of fitted parameters. Generally, values $\xi \leqslant 1$ indicate a statistically good fit. However, because of possible uncertainty in both the observations and the model (such as data selection by the simplified ionization function I; see Section 2.1), we accept values slightly larger than unity as reasonable.

We use the highly efficient Bayesian analysis search of the admitted solutions in the parameter space as described by the multimode nested sampled method efficiently implemented by the `MultiNest` code (e.g., Feroz 2008; Feroz et al. 2009). The different nature of the adjustable parameters in our model adds a slight complication in our effort. This is because while the SFD parameters (α, β, $D_{\rm mid}$, N_0) and the particle production parameter γ project onto the results in a deterministic way, the effect of the collisional lifetime adjustment parameter $F_{\rm coll}$ is statistical in nature. As mentioned in Section 3.3, the collisional breakup of the particles is a random process. A single simulation has stochastic variations, so we always perform 25 different runs for the same $F_{\rm coll}$ and average the results. This part is computationally demanding, because it needs to follow the orbital evolution of hundreds of thousands of particles from our integration output files. In fact, we opted to pre-compute the modeled distributions of impact speeds and orbital elements for each of the particle sizes and a grid of (γ, $F_{\rm coll}$) values. These results are then combined in the fitting model when trying to constrain the SFD parameter. In this way the SFD parameters are analyzed separately from the (γ, $F_{\rm coll}$). While the Markov chain walking is applied to the (α, β, $D_{\rm mid}$, N_0) parameter space, or alternately (α, β, $D_{\rm mid}$, $F_{\rm imp}$), the grid of (γ, $F_{\rm coll}$) is sampled uniformly within some preset values. The inconvenience is that no correlation of (γ, $F_{\rm coll}$) with the four SFD parameters is obtained, but we accept this limitation for simplicity.

4. MODEL: SYNTHETIC DATA AND COMPARISON WITH THE AVAILABLE OBSERVATIONS

4.1. Testing the Parameter Dependence of the Results

Before we present of our final results, we describe the most important global trends found when changing principal parameters. This helps better understand the problems and the parameter dependencies.

First, we consider separately runs with particles of a different size D and observe how they potentially contribute to the NT source. Figure 5 shows the synthetic population of NT particles for $D = 200\,\mu$m when no limiting cutoff of the ionization factor I is assumed (i.e., $I_\star = 0$). No collisional disruptions were modeled in this test. This reveals the potential impacting population of particles from HTCs as if the instrument had infinite sensitivity and the particles were indestructible (limited only by the dynamical transport from their ultimate source). To the zero order, the results match the observed population of NT particles (Figure 3), including the most prominent feature, the predominance of particles on orbits with low eccentricities. This is caused by a combination of the particle-orbits' ability to decouple from Jupiter (Section 3.2), and efficient circularization by PR drag. Since a reasonable SFD would favor small particles more than large ones, we consider the result to be promising.

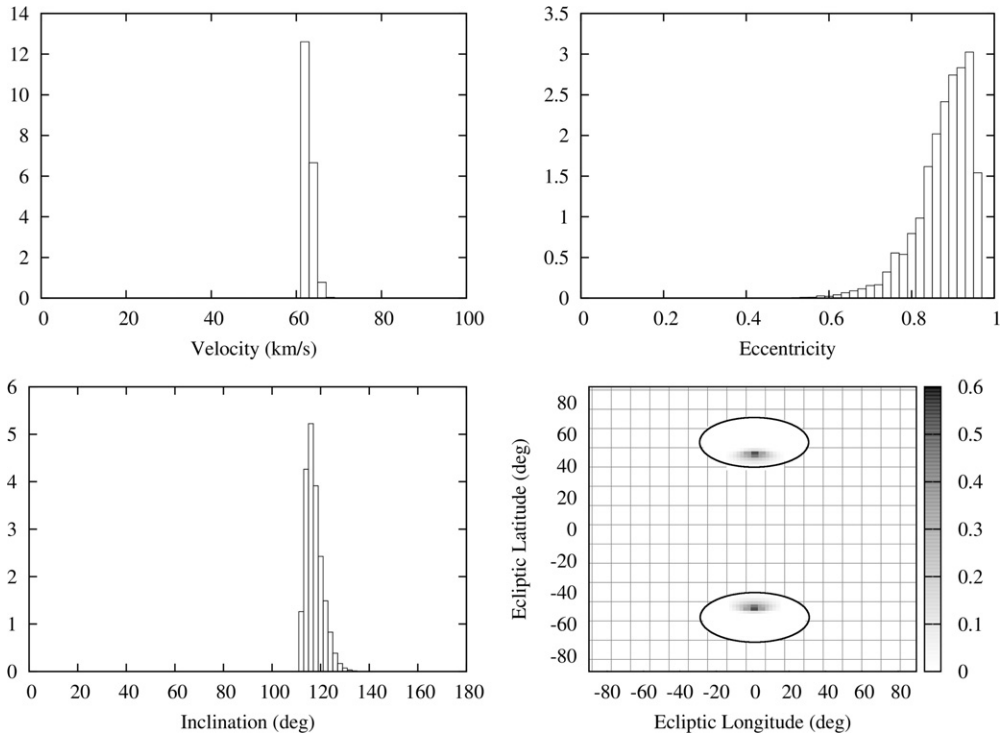

Figure 6. Same as in Figure 5, but now the lower cutoff of the ionization factor I is set to unity ($I_\star = 1$). Only a negligible tail population of particles impacting the Earth satisfy the ionization cutoff criterion $I \geqslant I_\star$, namely atypical orbits with high e and i values (both implying high impact speeds). Because of required high-inclination orbits, the radiants are shifted to lower latitudes. None of these features is compatible with the parameters of the observed NT particles (Figure 3).

However, the limited instrument sensitivity—as expressed here by the minimum ionization factor needed for detection—complicates these first results. Figure 6 is similar to Figure 5 but now takes into account the $I_\star = 1$ limit. Small masses and predominantly low impact velocity made most of the particles contributing to the signal in Figure 5 undetectable with this ionization factor cutoff. What remains is just the high-speed tail of particles impacting from retrograde and high-eccentricity orbits, which are not typical in the population. Moreover, the signal seen in Figure 6 is now not compatible with the observations and this leads to a potential problem. If the SFD of the impacting particles steeply increased toward small sizes (i.e., the weighting factor W_d large enough for $\leqslant$200 μm particles), even the tail contribution would corrupt the model. This puts a severe constraint on the slope β of the SFD (see Section 2.1 for some hints).

Figure 7 shows the same exercise but now for larger particles with $D = 600\,\mu$m. Their nearly 30 times larger mass makes them overcome the $I_\star = 1$ cutoff, and all particles are potentially detected by the CMOR system. It is still very promising that even the $D = 600\,\mu$m particles decouple from Jupiter for the most part and circularize their orbits to $e \leqslant 0.4$ values. Interestingly, the eccentricity range between ~0.5 and ~0.8 is underpopulated. We believe this is a result of the Kozai–Lidov effect, which makes eccentricity and inclination oscillate in a correlated way. The NT zone requires high orbital inclination values, and this requires the eccentricities to be smaller. Above $e \sim 0.8$ the eccentricity distribution again slightly increases, which is the contribution of the population of particles freshly released from the parent HTCs and those lately scattered by Jupiter.

Next, we probe the importance of collisional disruptions of the particles. Figure 8 shows a simulation for $D = 600\,\mu$m particles exceeding the $I_\star = 1$ cutoff (as in Figure 7), but now their losses due to breakups on the way to the Earth are included. We consider a nominal collisional model by Steel & Elford (1986), and also extended particle lifetimes with $F_\mathrm{coll} = 1$ to 10. As expected, shorter lifetimes do not allow particles to evolve much from their initial orbits, pushing thus the typical eccentricities to large values. The inclination values are also discordant with the observations (being systematically larger), indicating that more dynamical evolution is needed to extend their range. This is likely due to scattering by Jupiter and effects of multiple secular resonances in the intra-Jovian region. Clearly, $F_\mathrm{col} \geqslant 10$ values are needed to match the observations (see also a similar results from Nesvorný et al. 2011b).

4.2. Fitting the Model to the Observations

We now attempt to estimate parameters of the synthetic model that would best match the selected observations shown in Figure 3. Before doing so, it is useful to comment on the special status of the population parameter N_0 (Section 3.4, alternately, the F_imp parameter). Having the absolute daily number of observed meteoroids, we may in principle, estimate the total population of HTC particles (thus N_0). However, there is a suite of additional factors which bias the observations, and each of them may add some uncertainty.

First, we selected data from only a $\simeq$1/9 fraction of the 2012 year. The collision probability W_c in the synthetic model normalized estimate is effectively to a year in length, so we have to account for this selection. Second, there is a visibility bias of the source zone on the sky as seen by CMOR (e.g., Campbell-Brown 2008). Luckily, the northern location of the NT source means it is nearly always visible from Canada. We ran a simple simulator of the observations, taking into account the latitude of the CMOR system, the location of the NT source on the sky, and Earth's revolution about the Sun, and found

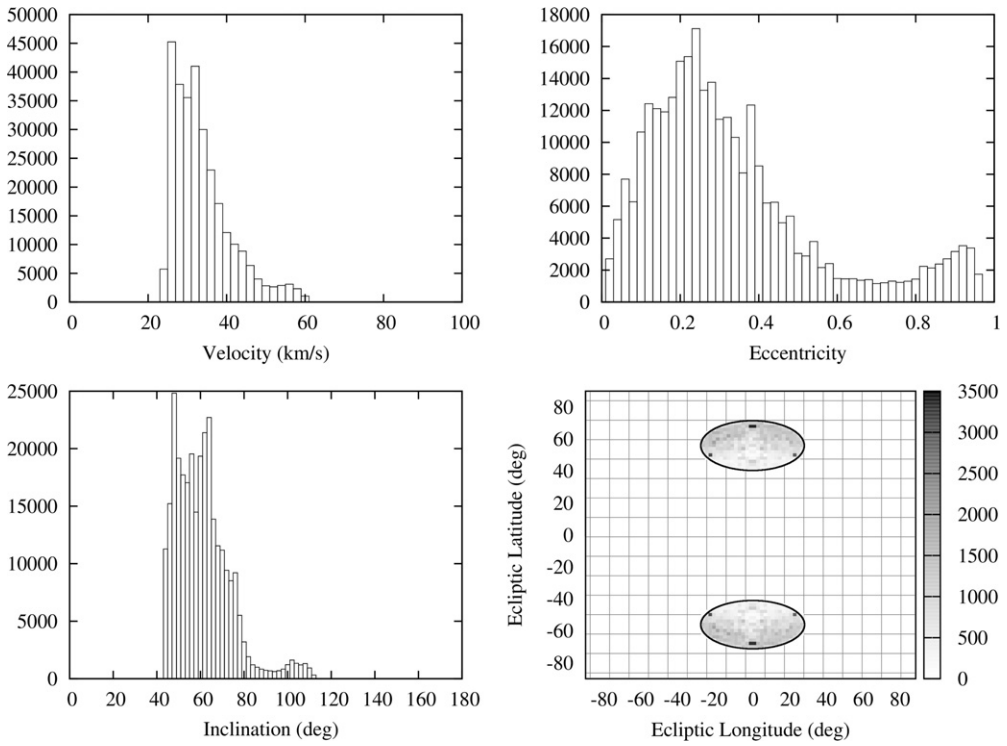

Figure 7. Same as in Figure 6, but now for particles of size $D = 600\,\mu$m. The corresponding figure for $I_\star = 0$ looks basically the same, indicating that virtually all 600 μm particle pass the ionization cutoff criterion for their typical impact speed of 30–40 km s^{-1}. The gross features of the distributions are now compatible with the parameters of the observed NT particles (Figure 3).

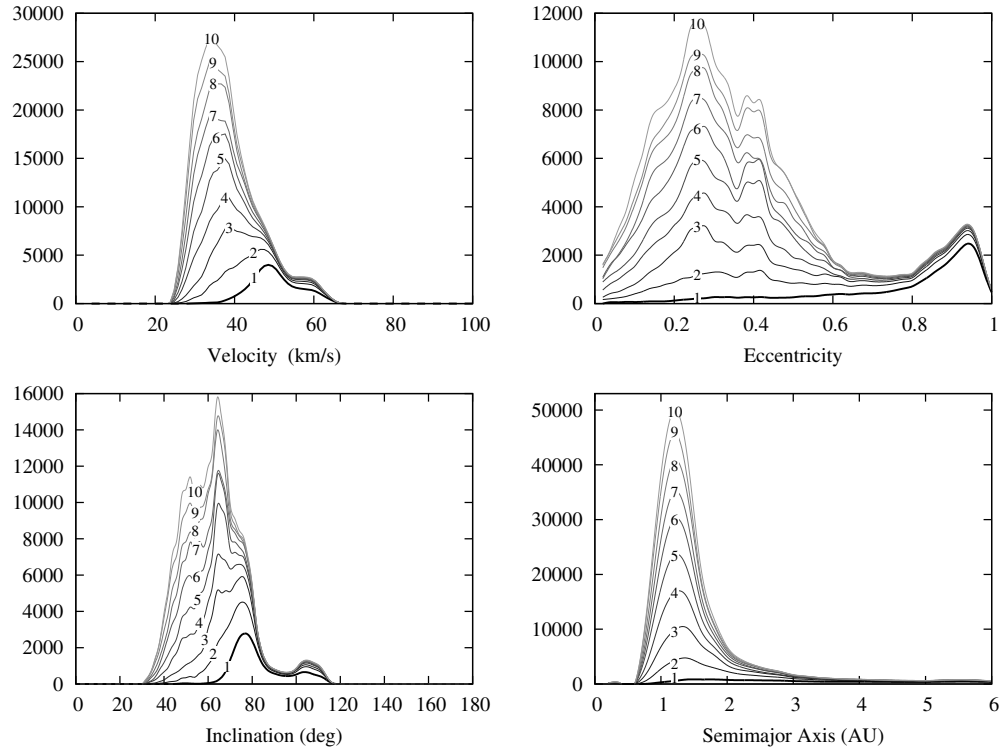

Figure 8. Same as in Figure 7, but now finite collisional lifetime of the particles is also modeled. The black line is for the nominal value of the collisional lifetime as given by the Steel & Elford (1986) model (i.e., $F_{\rm coll} = 1$). The sequence of gray lines assume longer collisional lifetime values than nominal by factors $F_{\rm coll} = 1$–10 from darker to lighter.

that the NT source region receives ≃40% visibility in the time interval we are using. We also used an actual collecting area for CMOR taking into account the true gain pattern of CMOR with mass index equal to 2. Most importantly, CMOR can effectively collect data from a limited surface area on the Earth (e.g., Brown & Jones 1995), while again the particle weighting W_c referred to impacts on the whole Earth surface. We estimate the ratio of the instantaneous surface area having detectable NT meteoroids ablating in the atmosphere as seen by CMOR and that of the Earth to be $\sim 6 \times 10^{-7}$, where the uncertainty of our estimate

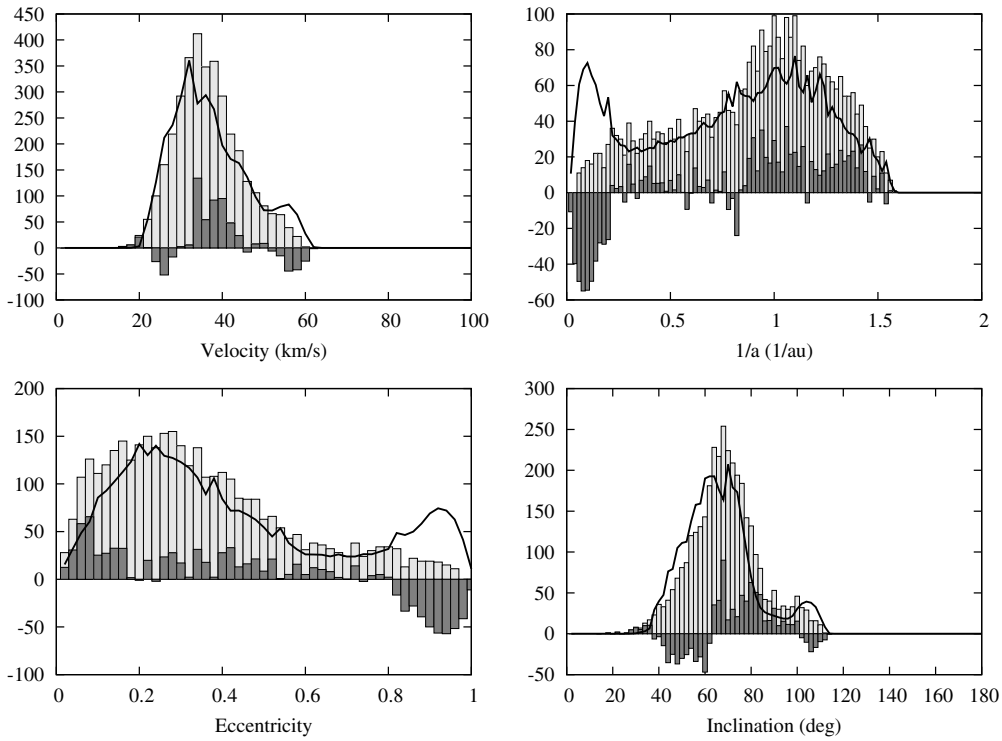

Figure 9. Comparison of the selected data set of NT meteoroids (gray histograms) with the results of our synthetic model (solid line) for the following set of parameters (broken power-law SFD model allowed): (α, β, $D_{\rm mid}$, $F_{\rm imp}$) = (4.7, 1.1, 950 μm, 1.08), γ = 0.0 (comet activity parameter, Equation (4)), and $F_{\rm coll}$ = 20 (fudge factor, by which we have to stretch the nominal values of the particle collisional lifetimes). The dark-gray filled histogram shows a difference between the observed and modeled signal in the particular bin. From this figure on, the semimajor axis a distribution has been replaced with a distribution of $1/a$ that contains a more detailed information.

is about an order of magnitude. We also apply a correction for echo height ceiling effect by multiplying our results by a factor of 2.5; according to (Section 6.5 in Campbell 2002) the NT meteors are detected with 35%–40% efficiency. Putting these factors together, CMOR can see in the spring months selected only 6.5×10^{-8} of the yearly load on the whole Earth. Therefore, we must apply this factor to recalibrate the fitted N_0 parameter in order to obtain information about the whole population of HTC particles.

In the course of testing our fitting procedure we also realized that it is not convenient, nor actually correct, to use semimajor axis distribution (see, e.g., Figure 3) of the impacting particles as a equal-weight data set. This is because the information in this parameter is too concentrated to the few bins around the 1–1.4 au range, while in other parameters, such as eccentricity, inclination and impact speed, the information is fairly distributed over a large range of values and thus data-bins. After experimenting with the data and model, we decided to fit $1/a$ rather than a of the impacting particles (see Figure 9, right and top panels). With that parameter, equivalent to the heliocentric binding energy, the information contained in the data expands and the model is, in fact, tested quite more severely than using simply the semimajor axis distribution.

We used a numerical code to search a parameter space with the limits[6] given in Table 1. As mentioned above, the (α, β, $D_{\rm mid}$, $F_{\rm imp}$) subspace was efficiently scanned by the Bayesian statistics procedure used by the `MultiNest` code, while the (γ, $F_{\rm coll}$) parameters were sampled with steps 0.1 and 5.

[6] For completeness we mention that we also probed an extended range for the β parameter down to negative values of −4 and found local minima of the χ^2 function for negative β values. Here we discard them, though, for lack of physical justification.

Table 1
Parameter Range in the Fitting Runs

Parameter	Minimum	Maximum
α	2.0	5.0
β	0.5	4.0
$D_{\rm mid}$	200 μm	1800 μm
$F_{\rm imp}$	0.8	1.2
γ	0.0	1.6
$F_{\rm coll}$	1	30

Notes. In the case of γ and $F_{\rm coll}$ parameters, for which we do not use the `MultiNest` search, we sample their values with 0.1 and 5 equal steps. Runs for each $F_{\rm coll}$ value were performed 25 times and results averaged to avoid flukes.

Our formally best solution with a broken power-law SFD was for (α, β, $D_{\rm mid}$, $F_{\rm imp}$) = (4.7, 1.1, 950 μm, 1.08), γ = 0.0 and $F_{\rm coll}$ = 20. The match to the data is shown in Figure 9. Overall, the fit is reasonable, matching the major features observed for NT meteoroids, there are, however, two major, and correlated, mismatches: our synthetic model provides an unobserved population of high-eccentricity and large semimajor axis orbits. Clearly, this is a population of freshly ejected particles that has still not evolved far from the HTC source orbits. Additionally, we find that the results only very weakly depend on the γ parameter but do depend on the $F_{\rm coll}$. As discussed above, values of $F_{\rm coll} \leqslant 5$ yield a synthetic model inconsistent with the data (Figure 8); $F_{\rm coll} \geqslant 10$ is needed, while values over 20 provide statistically equivalent results. Finally, our formal fit has a shallow SFD slope at the small-size end of the spectrum (i.e., β). The later seems somewhat puzzling, though hints are

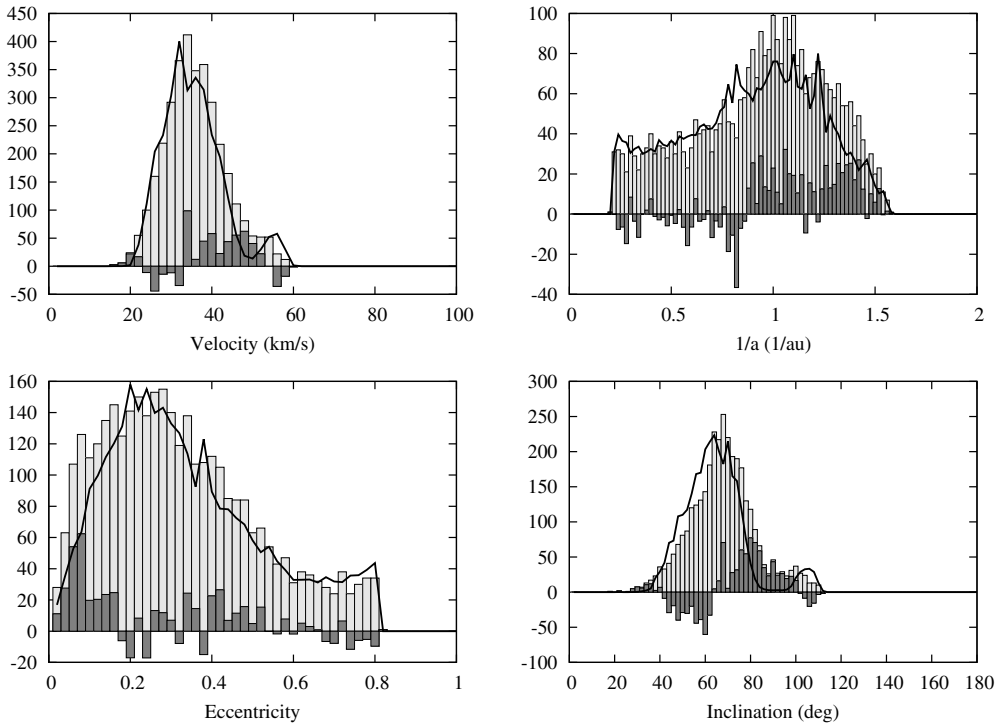

Figure 10. Same as in Figure 9, but now for the data set where all particles with observed heliocentric eccentricity values larger than 0.8 were eliminated. The best-fit parameters are $(\alpha, \beta, D_{\rm mid}, F_{\rm imp}) = (4.8, 1.6, 750\,\mu{\rm m}, 1.11)$, $\gamma = 0.3$ and $F_{\rm coll} = 20$.

already contained in the nature of the data set (see Section 2.1), and it is difficult to get around. The SFD break-point near to 1 mm and its shallow branch below this value has not been reported in any of the previous analyses.

While a "long collisional lifetime" of the particles is a required condition of satisfactory fits, we shall now test the sensitivity of the results with regards to two effects: (1) "selective-subjective" removal of the possibly undetected high-eccentricity orbits, and (2) necessity of the broken power-law SFD.

First, we note that the highest-speed particles are subject to more bias in the CMOR observations than the lower-speed particles (Section 6.5 in Campbell 2002). It may thus happen, that the "missing population" of the toroidal particles in the CMOR data, that we would predict from our synthetic model in Figure 9 (i.e., large-a and large-e heliocentric orbits), were removed (or were not detected) in the CMOR data and are not thus present in our final data set. To test this possibility, we rerun our fit on the data, where we artificially discarded all data with heliocentric eccentricity larger than 0.8 (where the data and models start to diverge in Figure 9). By doing this we obtained the results shown in Figure 10. The quality of fit improved, except for a small mismatch in the inclination fit (more lower-inclination particles predicted than observed and vice versa). From this test we conclude that the $e > 0.8$ particles may be incompletely detected, since the model otherwise fits the data well.

Now, we examine how much we can relax the shallowness of the particle SFD for small particles before the fit becomes worse. To that end we force the SFD be a single-slope power-law distribution with the exponent α in the range 1–5. Obviously, in this attempt we do not have the break-point size $D_{\rm mid}$ and the only fitted parameters, except for γ and $F_{\rm coll}$, are $(\alpha, F_{\rm imp})$ (the latter again standing for N_0). We used the CMOR data set where all particles with $e > 0.8$ were excluded as above. The best-fit model, $(\alpha, F_{\rm imp}) = (2.1, 1.11)$ with $\gamma = 0$ and $F_{\rm coll} = 20$, is formally worse in terms of χ^2 value than with the broken power-law SFD, but the visual check of the results we performed indicated no substantial differences. The top two panels in Figure 11 show the posterior distribution in Bayesian statistics of the α and $F_{\rm imp}$ parameters as determined by the `MultiNest` code. We also note the lack of correlation of the two parameters. Even when forcing α to be closer to a more realistic value between ~(2.8–3), we still get visually acceptable, though statistically worse fits. We recall that, given the simple nature of our treatment of the CMOR biases (such as a more complete understanding of the detection probability as a function of the ionization factor I and a complete treatment of the radar response function), a nominally statistically imperfect data fit may still be physically quite acceptable.

4.2.1. Total Mass of the Particle Population

With the population parameters estimated, we can now evaluate several interesting quantities. For instance, having the calibrated SFD parameters $(N_0, \alpha, \beta, D_{\rm mid})$ available, we can evaluate the total mass $M_{\rm tot}$ of the particles in the $(D_{\rm min}, D_{\rm max})$ range as (assuming both α and β smaller than 4)

$$\frac{M_{\rm tot}}{M_{\rm max}} = \frac{N_\alpha}{4-\alpha}\left[1 - \frac{\alpha-\beta}{4-\beta}\left(\frac{D_{\rm mid}}{D_{\rm max}}\right)^{4-\alpha} - \frac{4-\alpha}{4-\beta}\left(\frac{D_{\rm mid}}{D_{\rm max}}\right)^{4-\alpha}\left(\frac{D_{\rm min}}{D_{\rm mid}}\right)^{4-\beta}\right]. \quad (13)$$

We have assumed both α and β are smaller than a critical value of 4, and introduced mass $M_{\rm max} = \pi\rho D_{\rm max}^3/6$ of the largest particles with size $D_{\rm max}$ and bulk density ρ. Obviously, we may only expect to get an order of magnitude estimate because of several factors. First, the obtained parameters $(N_0, \alpha, \beta, D_{\rm mid})$ have large, and not fully established, uncertainties. Second, for slope exponents sufficiently smaller than 4, the largest particles dominate the mass, hence $M_{\rm tot} \sim M_{\rm max} N_\alpha/(4-\alpha)$. However,

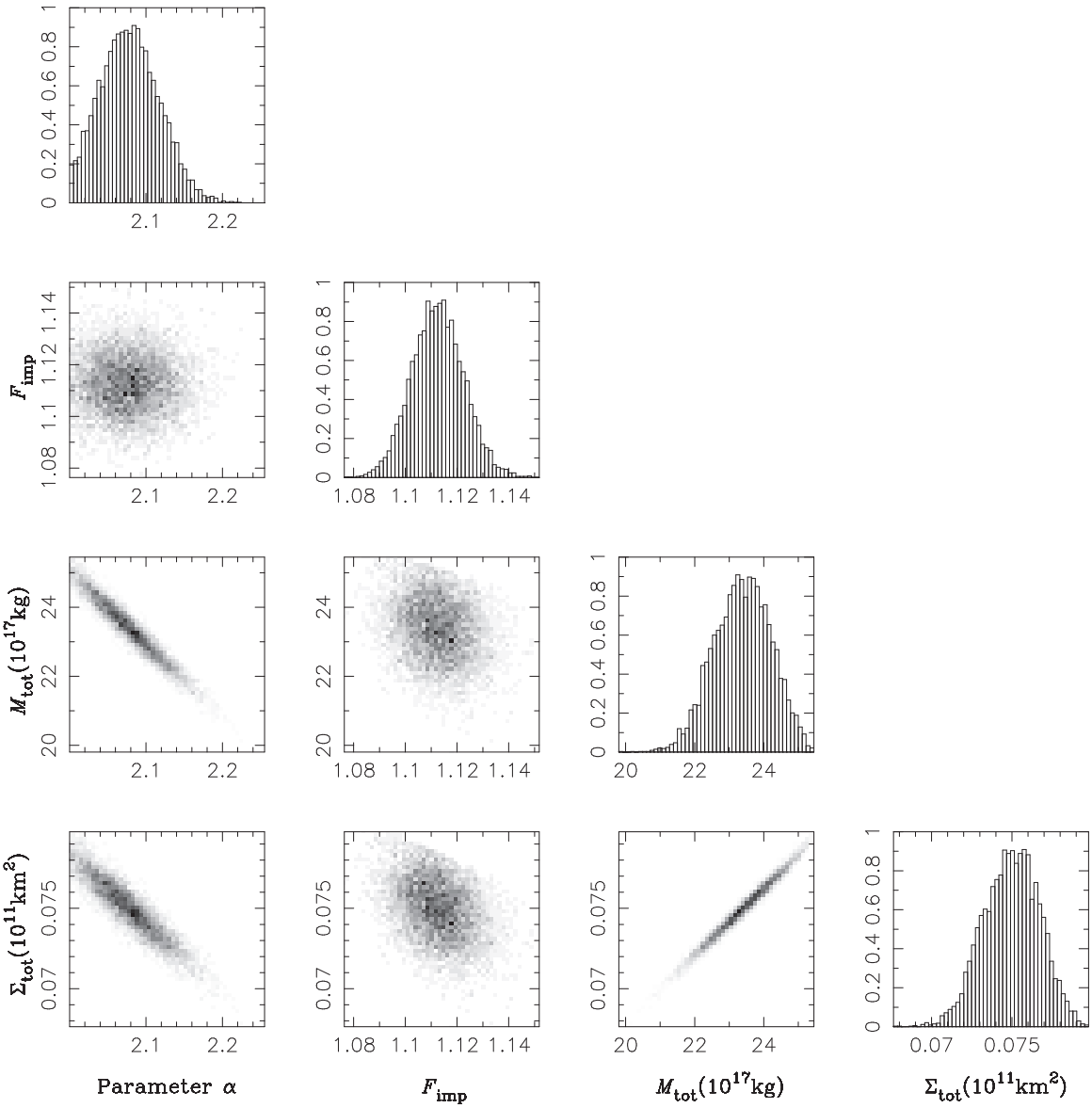

Figure 11. Posterior distribution of four parameters used in our model. Panels in the upper two lines show the fitted parameters α (SFD slope, top) and $F_{\rm imp}$ (population fudge factor, second line), with fixed values of $\gamma = 0$ and $F_{\rm coll} = 20$. Histograms in the outer plots show a distribution of statistically equivalent solutions, while the plot inside the triangular structure show projection of these solutions onto a two-dimensional planes of two selected parameters, where levels of gray scale represent density of solutions. This representation helps to understand possible correlations between the parameters. The bottom two rows show computed (using Equations (13)–(17)), not fitted, parameters discussed in Sections 4.2.1 and 4.2.2: (1) estimated mass $M_{\rm tot}$ of the steady-state HTC particle population in the interplanetary space within the fitted range ($D_{\rm min}$, $D_{\rm max}$) = (200 μm, 3 mm) (in 10^{17} kg; third row), and (2) estimated cross-section $\Sigma_{\rm tot}(\leqslant 5{\rm au})$ of the steady-state HTC particle population in the interplanetary space within the 5 au heliocentric distance (in 10^{11} km^2; bottom row).

these particles only weakly contributed to the model fit because of their small number. On the other hand, this approximation shows that the break-point location $D_{\rm mid}$ and the slope exponent β at smaller sizes only weakly influence the estimated mass $M_{\rm tot}$. This is well understood, because for shallow SFDs, the largest particles and the local slope of the SFD dominate the mass determination.

Since our formal solutions also admit $\alpha > 4$, we give here the population mass in this case (still assuming $\beta < 4$):

$$\frac{M_{\rm tot}}{M_{\rm mid}} = \frac{N_\alpha}{\alpha - 4}\left(\frac{D_{\rm max}}{D_{\rm mid}}\right)^{\alpha-1}\left[\frac{\alpha-\beta}{4-\beta} - \left(\frac{D_{\rm mid}}{D_{\rm max}}\right)^{\alpha-4} - \frac{\alpha-4}{4-\beta}\left(\frac{D_{\rm min}}{D_{\rm mid}}\right)^{4-\beta}\right], \quad (14)$$

with the mass of particles at the SFD break-point size now $M_{\rm mid} = \pi\rho D_{\rm mid}^3/6$ (obviously, the scaling uses the mass of the particles dominating the total mass of the population). The case $\alpha = 4$ would have to be treated separately, but we do not give the result here because of its singular nature in the α parameter solution.

Running formulas (13) and (14) through our solutions, we obtain $M_{\rm tot} \simeq (3\text{–}50) \times 10^{17}$ kg in our fitted particle size range between 200 μm and 3 mm. The third-row panel in Figure 11 gives the computed values of $M_{\rm tot}$ in the case where we fitted a single-slope power-law SFD. We note $M_{\rm tot}$ is anti-correlated with the slope parameter α, such that steeper-slope SFDs would yield smaller total particle mass $M_{\rm tot}$. This is easily understood because of by conservation of the number of impacting particles at the Earth.

With this order-of-magnitude estimate of HTC particle mass in interplanetary space, we can now attempt to constrain the long-term mass flux from HTCs needed to sustain the assumed steady-state population (for concepts of the flux computation see, e.g., Bottke et al. 2002, Section 4.3.1). Assuming a quasi-exponential decay of the population in our integrations with a characteristic timescale of $\tau \simeq 2$ Myr (Section 3.2), we need an average flux of

$$F = \frac{M_{\rm tot}}{\tau} \simeq (1.3\text{–}25) \times 10^{11} \text{ kg yr}^{-1} , \quad (15)$$

about an order of magnitude smaller than the mass influx estimated for the JFC population by Nesvorný et al. (2011a). This finding seems justifiable, since Nesvorný et al. (2010) found from the analysis of *IRAS* infrared observations of the zodiacal cloud that HTCs contribute about an order of magnitude less than JFCs at most. Similarly, the orbit-averaged activity of large HTCs is estimated to be $\sim(1\text{–}5) \times 10^9$ kg yr^{-1} (e.g., Hughes 1985; Jenniskens 2002). A steady-state population of several tens to a hundred of such comets would, in the long term, feed interplanetary space with sufficient dust for our findings. Additionally, modeling of direct dust detections beyond Jupiter requires a contribution from HTCs of about the same order of magnitude (e.g., Landgraf et al. 2002). These independent studies support our results and validate our approach.

4.2.2. Total Cross-section of the Particle Population

In a similar way, we may also estimate the total cross-section of the HTC-released population of particles in space. Assuming a particular case of $\alpha > 3$ and $\beta < 3$, we obtain

$$\frac{\Sigma_{\rm tot}}{\Sigma_{\rm mid}} = \frac{N_\alpha}{\alpha - 3} \left(\frac{D_{\rm max}}{D_{\rm mid}}\right)^{\alpha-1} \left[\frac{\alpha - \beta}{3 - \beta} - \left(\frac{D_{\rm mid}}{D_{\rm max}}\right)^{\alpha-3} - \frac{\alpha - 3}{3 - \beta} \left(\frac{D_{\rm min}}{D_{\rm mid}}\right)^{3-\beta}\right] , \quad (16)$$

where we have introduced $\Sigma_{\rm mid} = \pi D_{\rm mid}^2/4$, the cross-section of the particles at the break-point of the SFD. The assumed arrangement of the slope indexes for $D \geqslant D_{\rm mid}$ and $D \leqslant D_{\rm mid}$ makes these particles dominate the total cross-section. In fact, an order of magnitude estimate is given by $\Sigma_{\rm tot} \sim \Sigma_{\rm mid} N_\alpha (D_{\rm max}/D_{\rm mid})^{\alpha-1}/(\alpha - 3)$, and it is weakly sensitive to both extreme sizes, $D_{\rm min}$ and $D_{\rm max}$ in the spectrum.

Again, we formally need a total cross-section solution for $\alpha < 3$ (with $\beta < 3$), which reads

$$\frac{\Sigma_{\rm tot}}{\Sigma_{\rm max}} = \frac{N_\alpha}{3 - \alpha} \left[1 - \frac{\alpha - \beta}{3 - \beta} \left(\frac{D_{\rm mid}}{D_{\rm max}}\right)^{3-\alpha} - \frac{3 - \alpha}{3 - \beta} \left(\frac{D_{\rm mid}}{D_{\rm max}}\right)^{3-\alpha} \left(\frac{D_{\rm min}}{D_{\rm mid}}\right)^{3-\beta}\right] , \quad (17)$$

with $\Sigma_{\rm max} = \pi D_{\rm max}^2/4$. The critical value case $\alpha = 3$ is effectively not needed.

To compare our result to Nesvorný et al. (2010, 2011a) we also restricted the cross-section analysis to the population of particles with a heliocentric distance <5 au. For that purpose we went through the record of steady-state particle orbits used in our fitting procedure, and for each of them, evaluated a fraction of the orbit where the heliocentric distance was <5 au, and applied this factor to each individual orbit with an appropriate weight with which it contributes to the whole population. With that scheme our fitted particle populations provided $\Sigma_{\rm tot}(\leqslant 5\text{au}) \simeq (0.03\text{–}0.25) \times 10^{11}$ km^2, which is 1–2 orders of magnitude less compared to JFCs (Nesvorný et al. 2011a). The last-row panel in Figure 11 gives $\Sigma_{\rm tot}(\leqslant 5\text{au})$ in the fitting run with a single-slope SFD model.

4.3. HTC Contribution to Other Radiant Source Regions

So far, we have focused on the contribution of the HTC particles to the NT zone. However, these particles do not impact the Earth only in this radiant zone on the sky; rather, they contribute to other zones as well. Having calibrated our model, we can now estimate the contribution of HTC particles elsewhere.

It has long been suggested that the particles whose radiants are arranged in arc (or ring) structures at about 50° angular distance from the apex direction are related to the toroidal source (e.g., Wiegert 2008; Wiegert et al. 2009; Campbell-Brown & Wiegert 2009; Brown et al. 2010). These authors also noted that the structure is formed with the help of the Kozai–Lidov mechanism perturbing heliocentric orbits of the impacting particles. Indeed, assuming the Earth heliocentric orbit has zero eccentricity (and unitary radius) and denoting with δ the angular distance from the apex of a radiant for an impacting particle, we have

$$\cos\delta = \frac{1 - \sqrt{a}c}{\sqrt{3 - T(a, c)}} . \quad (18)$$

Here, we define $c = \cos i \sqrt{1 - e^2}$ and $T(a, c) = (1/a) + 2\sqrt{a}\, c$ with a, e and i being the heliocentric semimajor axis, eccentricity and inclination of the impacting particle orbit. Note that both c and T are conserved parameters of the Kozai–Lidov model (e.g., Kozai 1962). Obviously, a given orbit intersects the Earth at only a specific (and finite in number) radiants, but considering a set of orbits with slightly evolving a and c values, such as by the PR drag, the radiants will fill an arc structure characterized by a limited range of δ values.[7] Because the impact speed at infinity $V = \sqrt{3 - T(a, c)}$ is also nearly Kozai–Lidov-preserved, the observed impact speeds for the arc-radiant orbits are expected to be close to those observed in the NT source region. On the other hand, the individual orbital elements, especially eccentricity and inclination, undergo large variations and they are expected to have different distributions.

We have plotted the radiant distribution for all our modeled HTC particles and found a significant part of them populates the arc structure. Our model arc ensemble ranges from apex angular distances between $\delta \simeq 55°$ and about $\delta \simeq 65°$ bf (left panel in Figure 12), and is in a good agreement with all-sky observations made by CMOR in 2012 for solar longitudes between 50°–90° (right panel in Figure 12). Summarized all-sky observations were presented for instance, in Campbell-Brown (2008; see also Campbell-Brown & Wiegert 2009; Brown et al. 2010). We find that the depletion for δ smaller than our minimum value, described by Campbell-Brown (2008) as the depleted ring, is also due to the Kozai–Lidov mechanism. Equation (18) indicates that polar orbits with semimajor axis values between 1 and 2 au, which are most likely to hit the Earth, would have their radiants at $\simeq$ (45°–50°). However, these orbits are efficiently eliminated from our simulations en route to the inner solar system because

[7] We note that the Wyatt & Whipple (1950) integral for PR-evolving orbits implies that for a small c value a leading order relation reads $a \propto c^{-2}$. This means that δ changes only very moderately even if the orbits undergo large evolution driven by the PR drag.

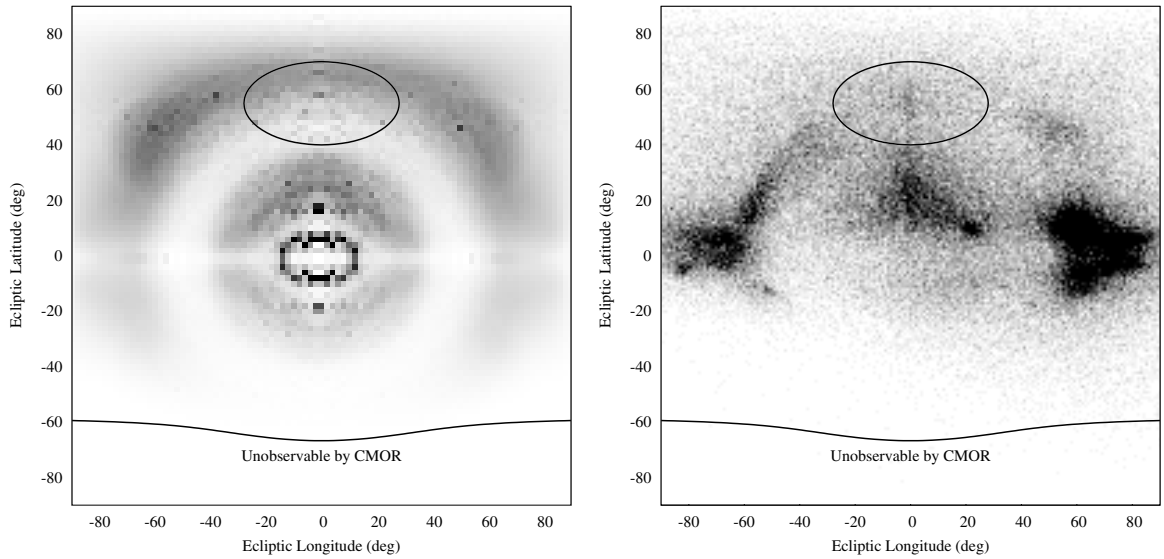

Figure 12. Distribution of radiant positions of our modeled population of micrometeoroids released from HTCs (left panel) and distribution of radiant positions of CMOR 2012 observations restricted to 50°–90° solar longitude (right panel); ecliptic longitude measured from the apex direction at the abscissa and ecliptic latitude at the ordinate. Gray-scale corresponds to the synthetic/observed particle flux. The oval zone centered at 57° ecliptic latitude indicates the NT region. We used our visibility simulator to compute a fraction of the year by which each of the latitude–longitude bin is observable from CMOR. This coefficient has been used to multiply the synthetic particle flux in each of the bins. The bottom solid curve delimits sky region that is not visible from CMOR at any time.

their perihelia would become too close to the Sun. In this way, our explanation for the depleted ring is mainly of a dynamical, rather than collisional, origin (see Campbell-Brown 2008). The few orbits whose radiants are seen in the zone of the depleted ring are prograde in nature and have mainly semimajor axis values smaller than 1 au and small eccentricities. They represent an unusual end-state, not efficiently fed by any evolutionary path and, obviously, they also have short collisional lifetimes. This is, however, only a secondary aspect of the depletion, the primary being dynamical origin.

While the impact speed distribution of arc orbits resembles that of the NT orbits (Figure 3), we see very different e and i distributions: (1) the median inclination is $\simeq$45° and extends from nearly zero to $\simeq$110°, and (2) the eccentricity distribution steadily increases to a value of $\simeq$0.8–0.9. The latter confirms our previous finding that very low e values in the NT source are the result of a selection effect: NT radiants simply require high inclination and the Kozai–Lidov dynamics then makes the eccentricity small. When the radiant-location is relaxed from the NT zone, the arc orbits have inclination distribution similar to the HTC orbits, with only slight preference for lower inclinations because of the higher collision probability with the Earth. The lower latitude radiants imply higher eccentricity values (e.g., Vokrouhlický et al. 2012).

We find that the HTC-released particles also contribute to the apex sources. Having $\delta \leqslant 30°$, they require predominantly retrograde or high eccentricity orbits. The first represents a minority of cases among our starting conditions for HTC-released dust particles, but retrograde orbits may be produced during their orbital evolution by scattering off Jupiter and/or the effects of secular resonances. With their larger impact speeds (median value $\simeq$55 km s^{-1} and a tail up to 70 km s^{-1}), the apex zone may see somewhat smaller particles than the NT zone. For instance, we find that particles between 100 and 200 μm contribute to the apex, while their input into the NT zone was negligible (Figure 1). For this reason it is problematic to use our calibrated population of the HTC particles and compute their exact flux at the apex zone (unless an uncertain extrapolation to smaller sizes is used). Since the impact speed, semimajor axis, eccentricity and inclination distributions from our 100 and 200 μm synthetic population resembles closely the observed data (see, e.g., Campbell-Brown 2008), we find it promising that our model predicts the HTC particles are contributors to the apex zone too. Additionally, our simulations show that the average strength of the apex source is ~5 to ~15 times larger than the NT source and depends, among other factors, also on the γ exponent of the cometary dust production function (4). Since the NT signal is largely insensitive to γ, further work on how the HTC dust contributes both in NT and apex sources may help in refining our model. Re-evaluation of the relative weight at which this dust component and dust from new (Oort cloud) comets contribute at apex (as advocated by Nesvorný et al. 2011b), however, needs a separate, dedicated study. It would be advantageous to combine CMOR data with other radars that have different limiting sensitivity for instance the AMOR system (e.g., Galligan & Baggaley 2005) or the MU system (e.g., Kero et al. 2012).

4.4. Contribution to IR Flux of the Zodiacal Cloud

Nesvorný et al. (2010, 2011a) have calibrated the zodiacal cloud parameters using a combination of a dynamical model and infrared measurements from the *IRAS* spacecraft. In particular, they found that the total cross-section of the cloud inside Jupiter's orbit (heliocentric distances $\leqslant$5 au) is ~ (1–2) × 10^{11} km^2, with the dominant contribution from particles in the 100–200 μm size range. This is because they also used a broken power-law SFD with a $D_{\rm mid}$ value in this size interval.

Nesvorný et al. (2010) also included a model of the HTC dust contribution in the zodiacal cloud. Their HTC model, though somewhat simpler, was comparable to ours. They estimated that HTC dust contributes less than 10% in the quoted total cross-section. Because it is calibrated by an entirely different data set, it is interesting to check our solution for the HTC dust yields with their constraints. Note that this comparison is somewhat problematic, because out data are insensitive to the smallest

possible sizes contributing to the zodiacal cross-section. If anything, the cross-sectional estimate from our population must be even smaller than the mentioned 10% value.

In Section 4.2.2 we determined that our HTC particle populations that generally match the toroidal source provide $\Sigma_{\rm tot}(\leqslant 5\,{\rm au}) \simeq (0.03\text{–}0.25) \times 10^{11}$ km^2. This is indeed at most 10% of the JFC particle population cross-section found by Nesvorný et al. (2010). Hence our HTC particles should not cause a conflict in fitting the *IRAS* infrared measurements by providing inconsistently large cross-sections that would flatten latitudinal profiles of IR emission measured by *IRAS*. A more detailed modeling of the HTC dust contribution to the thermal emission of the zodiacal cloud is left for future work.

5. DISCUSSION AND CONCLUSIONS

We have shown that the steady-state population of toroidal meteoroids as observed by the CMOR radar is likely provided by the activity or breakups of HTCs. The model provides a constraint on several parameters, such as the mean comet activity in relation to the perihelion distance and parameters of the particle size distribution at the source in the ~200 μm–~3 mm size range.

A stronger constraint is imposed on the collisional lifetime of particles in the millimeter size range. In order to dynamically transport particles to the vicinity of the Earth, we find that our model requires a longer lifetime than predicted by standard models (e.g., Grün et al. 1985). We think there are several possibilities to explain this difference. For example, we do not take into account fragments from collisional disruptions of the particles on their way toward the inner parts of the solar system. The resulting collisional cascade may effectively extend the lifetimes of their parent particles.

Another possible solution is to accelerate the dynamical evolution of the particle orbits. For instance, we assumed particle bulk density of 2 g cm^{-3}, but if the cometary dust has a lower value the orbits would evolve faster. It is also possible that a more in-depth analysis of the solar wind interaction with microscopic particles at large heliocentric distances may exceed this canonical value and contribute thus to faster orbital decay.

Finally, we note that several measurements of the lifetime of cosmic spherules and interplanetary dust particles (e.g., Raisbeck & Yiou 1989; Olinger et al. 1990; Nishiizumi et al. 1991; Pepin et al. 2001; Kehm et al. 2006) suggest the ultimate resolution to this dilemma may simply be that meteoroid collisional lifetimes are longer than previously assumed. Some of the residual mismatches between the observed data and our model may also originate in our ability to describe the detection limits of the radar system. In this work, similar to previous workers, we used the simple ionization factor I defined in Equation (1) to characterize the detectability of the modeled impacting particles. This captures the most important features, such as the particle's ability to ionize the atmospheric constituents, but may disregard others. Most importantly, we suspect that the instantaneous change from non-detectability to detectability at a single value $I_\star = 1$ is too simplified. In reality, there should be a range of I values about this critical limit where a particle detection should be a probabilistic event with the probability slowly increasing from zero (at small I) to unity (at large I). We believe that having the ability to properly model this feature would also improve fits with single power-law SFD, since the SFD break and small β values formally found in Section 4.2 is just another face of the same problem. Additionally, the need to disregard high-eccentricity orbits ($e \geqslant 0.8$) in our best fits is likely related to preferential rejection of those inputs from the data set.

Our next efforts will focus on two projects related to this work. First, we shall analyze the time-variable component in the NT source (Figure 2) searching for possible individual sources (if they still exist and are known in our catalogs). The prime candidate for some, but not all, is the activity of the peculiar comet 96P/Machholz and the complex of related objects (e.g., Sekanina & Chodas 2005). Second, the results of this paper motivate us to revisit dynamical modeling of the origin of apex source particles. Nesvorný et al. (2011b) found that dust released from new (Oort cloud) comets may contribute to this region. Unsurprisingly, we find that this is so for the dust released from HTCs as well. The exact proportion of these two potentially contributing source populations of dust is, however, yet to be determined.

This research was supported by Czech Grant Agency and the Grant Agency of the Charles University (grants P209-13-01308S, SVV-260089, and GAUK 602213). The work of D.N. was supported by NASA's PGG Program. CMOR measurements were supported by funding from NASA's Meteoroid Environment Office through co-operative agreement NNX11AB76A. The work of M.C.B. and P.B. were supported by the Natural Sciences and Engineering Research Council of Canada and the Canada Research Chairs program.

APPENDIX

PRELIMINARY ANALYSIS OF CMOR DATA SET

In order to gain more understanding of the data, and to set the stage for construction of the full model in Section 3, we additionally performed the following simple test. We randomly sampled the NT radiant sky zone and associated with it an impacting particle with a speed modeled by a Gaussian distribution (no correlation between the radiant and the impact speed was assumed). The Gaussian distribution was characterized with two parameters, namely, (1) a mean value $V_{\rm g}$, and (2) a standard deviation $\delta V_{\rm g}$. Having chosen the radiant and impact speed, we easily obtain the necessary heliocentric orbital elements for computation of the related impact probability $P_{\rm coll}$ of this synthetic impactor (e.g., Vokrouhlický et al. 2012). Next we characterized the impactor population with a broken power-law SFD described in Section 3.4 below in the size range $(D_{\rm min}, D_{\rm max}) = (200, 3000)\,\mu$m. This brings another three parameters, notably (1) size $D_{\rm mid} \in (D_{\rm min}, D_{\rm max})$ at which the power-law index changes, and (2) power-law indexes α and β of the two slopes (parameter N_0 from SFD definition in Section 3.4 is fixed by the absolute number 3550 of selected background-population NT particles). With this simple model we fit (1) the observed velocity distribution from Figure 3, and (2) the observed size distribution of the NT-impacting particles (note that this is different from the SFD fitting in Section 3 where we consider parameters at the source rather than those of the impacting population on the Earth). In fact, the latter was computed from the reported mass distribution using a constant bulk density of 2 g cm^{-3}. Obviously, the $(V_{\rm g}, \delta V_{\rm g})$ adjustment basically follows from the velocity-distribution fit and $(D_{\rm mid}, \alpha, \beta)$ adjustment basically follows from the size distribution fit, but the fitting procedure is not uncorrelated. This is because we only accept particles that could have been detected by CMOR, by constraining the ionization factor I of the impacting synthetic particle to be higher than the $I_\star$ limit described above.

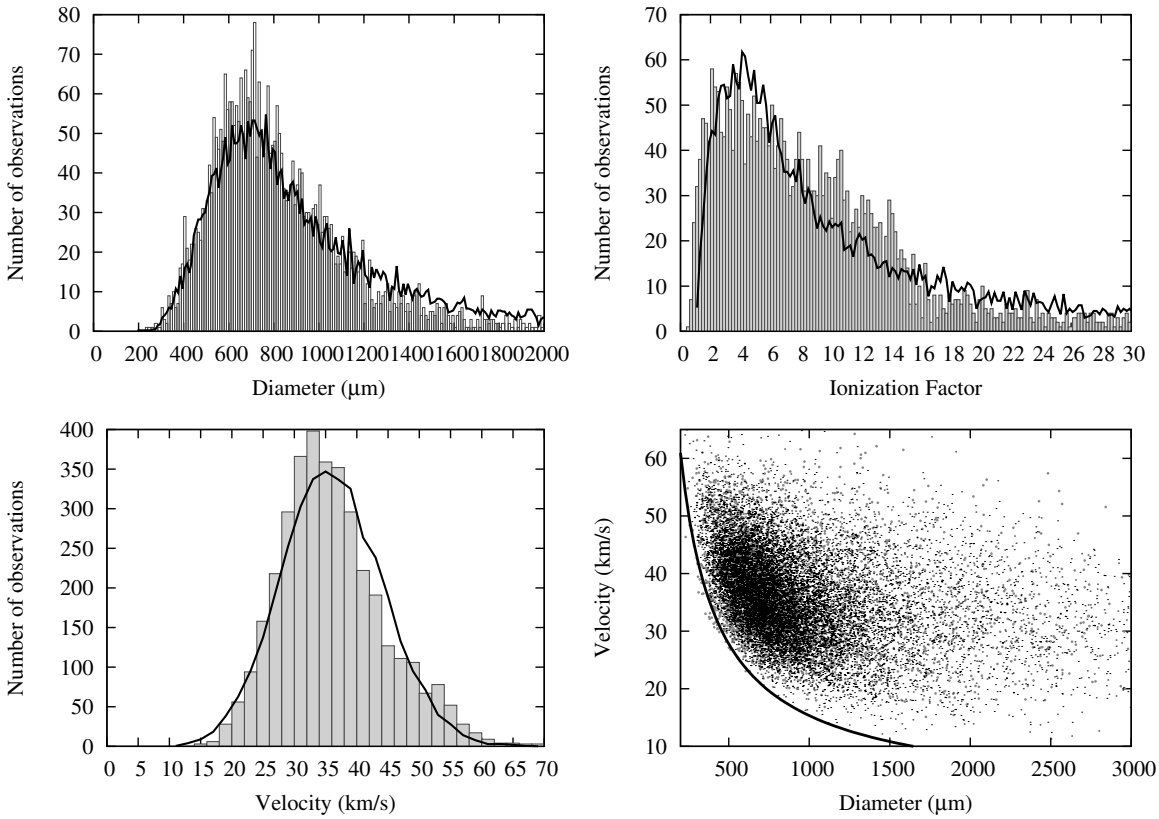

Figure 13. Results from a simple, five-parameter fitting analysis described in Section 2.1: gray histograms are for 3550 observed particles from the background population of NT particles, black line is the adjusted model. Left panels show the fitted data, size distribution of the particles (top), and geocentric impact speed (bottom). Both are matched very well by the model. The top right panel shows a comparison of the data and the model for the ionization factor I; here a slight mismatch is seen at low I values. The bottom right panel shows the observed particles (black symbols) and modeled particles (gray symbols) projected onto the size vs. velocity plane.

The results are shown in Figure 13. Unsurprisingly, the velocity fit is fairly good with only a small mismatch due to a large-velocity tail in the observed distribution (related to a small contribution of retrograde impactors from Figure 3). The adjusted values read $V_g = 31.8 \pm 0.3$ km s^{-1} and $\delta V_g = 9.2 \pm 0.3$ km s^{-1}. The fit of the observed size distribution is also rather good (the normalized χ^2 parameter from Equation (12) is $\sim$0.8). The formal solution of the adjusted parameters is $D_{\rm mid} = (750 \pm 20)\,\mu$m, $\alpha = 3.0 \pm 0.1$ and $\beta = 1.0 \pm 0.2$. Of these values, only α matches the expected value (see references in Section 3.4), while the value β is quite shallow and the break-point at $\simeq$750 μm has not been reported in the literature. Recall that the observed-population SFD maps to the source-population SFD in a non-trivial way due to size-dependent dynamical (PR drag) and physical (collisional lifetime) effects. However, understanding of some elements of the model may not be entirely correct, as indicated by the poor match between the distribution of the observed and modeled ionization factor (top left panel on Figure 13). This may be due to an unmodeled correlation between the radiant position and impact speed (which is, however, not strongly seen in the data). The problem may, however, also be deeper and indicate that (1) either the ionization factor from (1) is just too simplified, and does not accurately capture all the fine details of particle detections, or (2) the sharp transition from non-detected to detected particles as I crosses the critical value $I_\star = 1$ is unrealistic. The latter issue (2) is an especially important factor in our opinion. In fact, there should be some interval of ionization factor values, say between 1 and 3–5, where particles are detected with a probability smaller than unity (increasing toward the larger I values). This may well explain why we are forced to assume the shallow distribution below the break-point $D_{\rm mid}$ in our simple test. However, at this moment we do not have available an in-depth analysis of detection efficiency as a function of I near the critical value $I_\star$, nor a replacement of I with another quantity that would more realistically capture the particle detectability. With such warnings we thus proceed toward the full numerical model for the background population of the NT particles. We should note, that the break-point may be related to the simplified nature of the mass determination, in particular in the intermediate scattering region between underdense and overdense echoes that are treated as a step function rather than through a full-wave model approach such as Poulter & Baggaley (1978). Refinements in the radar mass scale in future may change the results, but the general mechanics of our model should not be significantly affected.

REFERENCES

Blaauw, R. C., Campbell-Brown, M. D., & Weryk, R. J. 2011, MNRAS, 412, 2033
Bottke, W. F., Morbidelli, A., Jedicke, R., et al. 2002, Icar, 156, 399
Brown, P. G., & Jones, J. 1995, EM&P, 68, 223
Brown, P. G., Weryk, R. J., Wong, D. K., & Campbell-Brown, M. D. 2012, DPS, 44, 302.04
Brown, P. G., Weryk, R. J., Wong, D. K., & Jones, J. 2008, Icar, 195, 317
Brown, P. G., Wong, D. K., Weryk, R. J., & Wiegert, P. 2010, Icar, 207, 66
Campbell, M. D. 2002, PhD thesis, Univ. Western Ontario (Canada)
Campbell-Brown, M. D. 2008, Icar, 196, 144
Campbell-Brown, M. D., & Wiegert, P. 2009, M&PS, 44, 1837

Čapek, D., & Vokrouhlický, D. 2010, A&A, 519, A75
Chau, J. L., Woodman, R. F., & Galindo, F. 2007, Icar, 188, 162
Davies, J. G. 1957, in IAU Symp. 4, Radio Astronomy, ed. H. C. van de Hulst (Cambridge: Cambridge Univ. Press), 390
Davies, J. G., & Gill, J. C. 1960, MNRAS, 121, 437
Dermott, S. F., Grogan, K., Durda, D. D., et al. 2001, in Orbital Evolution of Interplanetary Dust, ed. E. Grün, B. A. S. Gustafson, S. Dermott, & H. Fechtig (Berlin: Springer), 569
Feroz, F. 2008, PhD thesis, Cambridge Univ.
Feroz, F., Hobson, M. P., & Bridges, M. 2009, MNRAS, 398, 1601
Fulle, M. 2004, in Motion of Cometary Dust, ed. M. C. Festou, H. U. Keller, & H. A. Weaver (Tuscon, AZ: Univ. Arizona Press), 565
Galligan, D. P., & Baggaley, W. J. 2005, MNRAS, 359, 551
Gonczi, R., Rickman, H., & Froeschle, C. 1992, MNRAS, 254, 627
Greenberg, R. 1982, AJ, 87, 184
Grün, E., Zook, H. A., Fechtig, H., & Giese, R. H. 1985, Icar, 62, 244
Hashimoto, T., Watanabe, J., Sato, M., & Ishiguro, M. 2011, in Meteoroids: The Smallest Solar System Bodies, ed. W. J. Cooke, D. E. Moser, B. F. Hardin, & D. Janches (Washington, DC: NASA), 82
Hawkins, G. S. 1956, AJ, 61, 386
Hawkins, G. S. 1962, AJ, 67, 241
Hawkins, G. S. 1963, SCoA, 7, 53
Hughes, D. W. 1985, MNRAS, 213, 103
Jenniskens, P. 2002, in ESA Special Publication, Vol. 500, Asteroids, Comets, and Meteors: ACM 2002, ed. B. Warmbein (Noordwijk, Netherlands: ESA), 117
Jenniskens, P. 2006, Meteor Showers and their Parent Comets (Cambridge: Cambridge Univ. Press)
Jenniskens, P. 2008a, EM&P, 102, 505
Jenniskens, P. 2008b, Icar, 194, 13
Jewitt, D., Li, J., & Agarwal, J. 2013, ApJL, 771, L36
Jones, J., & Brown, P. G. 1993, MNRAS, 265, 524
Jones, J., Brown, P. G., Ellis, K. J., et al. 2005, P&SS, 53, 413
Jones, J., Campbell, M., & Nikolova, S. 2001, in Proceedings of the Meteoroids 2001 Conference, ed. B. Warmbein (ESA SP-495; Noordwijk: ESA), 575
Jones, J., & Jones, W. 1993, MNRAS, 261, 605
Kaňuchová, Z., & Neslušan, L. 2007, A&A, 470, 1123
Kehm, K., Flynn, G. J., & Hohenberg, C. M. 2006, M&PS, 41, 1199
Kero, J., Szasz, C., Nakamura, T., et al. 2012, MNRAS, 425, 135
Kessler, D. J. 1981, Icar, 48, 39
Kozai, Y. 1962, AJ, 67, 591
Landgraf, M., Liou, J.-C., Zook, H. A., & Grün, E. 2002, AJ, 123, 2857
Levison, H. F., & Duncan, M. J. 1994, Icar, 108, 18
Levison, H. F., Duncan, M. J., Dones, L., & Gladman, B. J. 2006, Icar, 184, 619
Nesvorný, D., Janches, D., Vokrouhlický, D., et al. 2011a, ApJ, 743, 129
Nesvorný, D., Jenniskens, P., Levison, H. F., et al. 2010, ApJ, 713, 816
Nesvorný, D., Vokrouhlický, D., Bottke, W. F., & Sykes, M. 2006, Icar, 181, 107
Nesvorný, D., Vokrouhlický, D., Pokorný, P., & Janches, D. 2011b, ApJ, 743, 37
Nishiizumi, K., Arnold, J. R., Fink, D., et al. 1991, E&PSL, 104, 315
Olinger, C. T., Walker, R. M., Hohenberg, C. M., & Maurette, M. 1990, E&PSL, 100, 77
Öpik, E. J. 1951, PRIAA, 54, 165
Pepin, R. O., Palma, R. L., & Schlutter, D. J. 2001, M&PS, 36, 1515
Pokorný, P., & Vokrouhlický, D. 2013, Icar, 226, 682
Poulter, E. M., & Baggaley, W. J. 1978, P&SS, 26, 969
Press, W. H., Teukolsky, S. A., Vetterling, W. T., & Flannery, B. P. 2007, Numerical Recipes. The Art of Scientific Computing (3rd ed.; Cambridge: Cambridge Univ. Press)
Raisbeck, G. M., & Yiou, F. 1989, Metic, 24, 318
Sekanina, Z., & Chodas, P. W. 2005, ApJS, 161, 551
Steel, D. I., & Elford, W. G. 1986, MNRAS, 218, 185
Verniani, F. 1973, JGR, 78, 8429
Vokrouhlický, D., Pokorný, P., & Nesvorný, D. 2012, Icar, 219, 150
Weryk, R. J., & Brown, P. G. 2012, P&SS, 62, 132
Wetherill, G. W. 1967, JGR, 72, 2429
Wiegert, P., Vaubaillon, J., & Campbell-Brown, M. 2009, Icar, 201, 295
Wiegert, P. A. 2008, EM&P, 102, 15
Wyatt, S. P., & Whipple, F. L. 1950, ApJ, 111, 134